Book of Proceedings

Seventh Workshop

"Solar Influences on the Magnetosphere, Ionosphere and Atmosphere",

Sunny Beach, Bulgaria, 1-5 June 2015

Organized by:

Space Research and Technologies Institute
Bulgarian Academy of Sciences

Scientific Organizing Committee

Editors: **Katya Georgieva, Boian Kirov, Dimitar Danov**

CONTENT

CONTENT

Solar Cosmic Ray Acceleration and Propagation

I. M. Podgorny[1], *A. I. Podgorny*[2]

[1] Institute for Astronomy RAS, Moscow, Russia,
[2] Lebedev Physical Institute RAS, Moscow, Russia
E-mail: podgorny@inasan.ru

Abstract.

The GOES data for the flare proton energies of 10 - 100 MeV are analyzed. Proton fluxes ~ 10^{32} acceleration takes at the current sheet decay. Proton acceleration of in a flare occurs along a singular line of the current sheet by the Lorentz electric field, as in the pinch gas discharge. The pulse of protons duration is by 2 - 3 orders of magnitude longer than the duration of flares. The high-energy proton flow from the flares that appear on the Western part of the solar disk arrive to Earth with the time of flight. These particles propagate along magnetic lines of the Archimedes spiral connecting the flare with the Earth. Protons from the flare on the Eastern part of the solar disk begin to register with a delay of more than three hours. Such particles cannot get on the magnetic field line connecting the flare with the Earth. These protons reach the Earth, moving across the interplanetary magnetic field. The particles captured by the magnetic field of the solar wind are transported with solar wind and due to diffusion across the magnetic field. The patterns of solar cosmic rays generation demonstrated in this report are not detected during the small ($\Phi \le 1$ см$^{-2}$ с$^{-1}$ стер$^{-1}$) proton events.

Introduction

About 30% of big flares (class X and even less class M) are accompanied by a flux of relativistic protons. Part of these protons hits the Sun and causes nuclear reactions. The other part of the protons propagates into the interplanetary medium. Despite decades of the effort, the relativistic flare protons remain the least studied manifestation of the flare [1]. The energy of the charged particles in the interplanetary plasma can change only due to the emission or movement along the electric field $Md\mathbf{V}/dt = e\mathbf{E} + e[\mathbf{V}\times\mathbf{B}]/c$. The change of the energy of a particle moving in the field is $dW = eE_r dr$. The electric field may be of different origin: the field of another charged particle (at a collision), space charge field, in particular due to polarization of charges in the plasma, the field induction dB/dt, etc. At the scattering by inhomogeneities of the magnetic field the particle can change the energy only due to motion in the electric field associated with a magnetic field fluctuation. This was clearly articulated in the well known work of Berezhko E. G., and Krymsky G. F. [2]: "Possibility of charged particles acceleration in the plasma in the related electric fields." The change of the energy at scattering by a magnetic fluctuation is determined by the magnitude and spatial scale of the electric field in such fluctuations

Two possibilities of solar cosmic rays generation are discussed in the literature:

a). Proton acceleration in the Lorentz electric field $\mathbf{E}_{rec} = -\mathbf{V}_{rec}\times\mathbf{B}_{cs}/c$ along the singular lines (in particular the line B=0) in the current sheet during magnetic reconnection [3, 4]. Here, $\mathbf{V}_{rec}$ – the velocity of magnetic reconnection, $\mathbf{B}_{cs}$ – the magnetic field of the decaying current sheet. The scheme of proton acceleration in a flare current sheet is shown in fig. 1. The maximum energy of the protons accelerated in the current sheet of a solar flare can be estimated as follows. At a typical velocity of reconnection in a flare is $V_{rec} = 2\times10^7$ cm/s, the magnetic field in the current sheet is $B_{cs} = 100$ G, and the length of the sheet is $L \sim 10^9$ cm the maximum energy of protons accelerated in the current sheet, can be estimated as $W = L\, V_{rec}B_{cs}/c \sim 20$ GeV. This estimation is corresponded to the maximum energy of protons measured at a flare by neutron monitors [5 - 7].

b). Fermi acceleration by the Lorentz electric field $\mathbf{E}_{shock} = -\mathbf{V}_{shock}\times\mathbf{B}_{shock}/c$, in a shock wave, contained the magnetic field. Here, $\mathbf{V}_{shock}$ and $\mathbf{B}_{shock}$ - the velocity and the magnetic field

of the shock wave. The scheme of Fermi acceleration is shown in fig. 2a. Getting to area of a magnetic cloud (shock) that moving towards with the velocity V, the particle moves along a part of the Larmor circle and gains the energy $\delta W = 2\rho Ee$ in the Lorentz electric field. Here, ρ is the Larmor radius. As a result of reflection, the particle velocity increases on $2V_{shock}$. If the particle is captured between two moving to each other magnetic clouds, such particle gains energy at each reflection.

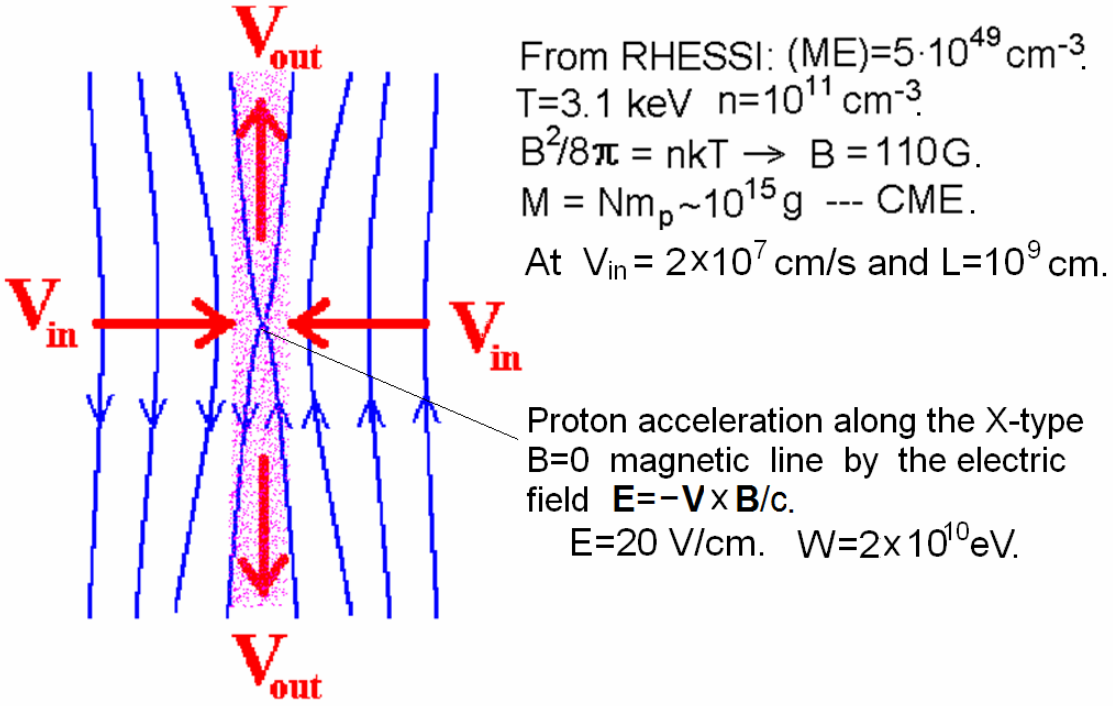

Fig. 1. The plasma velocity vectors and magnetic field lines in the current sheet at reconnection. The electric field -V×B/c is directed perpendicular to the figure plane .

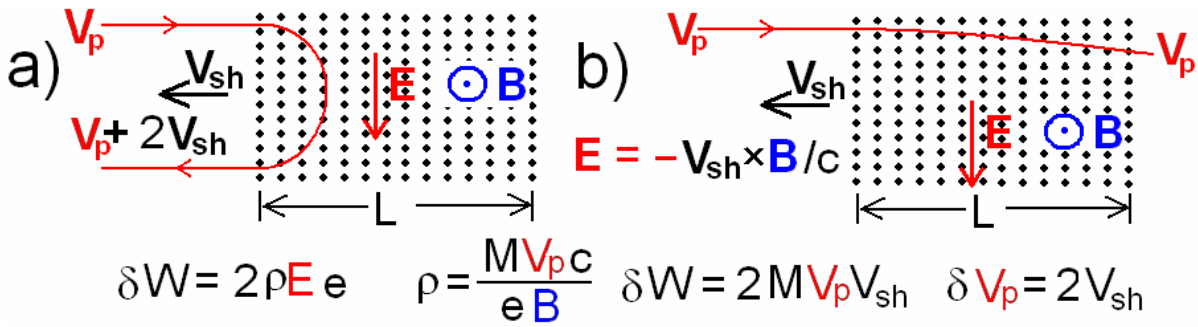

Puc. 2. a). The scheme of the Fermi acceleration of the first type. b). Drift is impossible for particles, if the Larmor radius has the larger size than magnetic cloud. The particle crosses the shock wave.

The maximum energy attainable at acceleration by the Fermi mechanism corresponds to the condition of equality of the Larmor radius to the size of the magnetic plasma cloud. At higher energy the proton drift in the magnetic field is impossible, and the particle crosses the magnetic cloud. It cannot be accelerated in the field of Lorentz field to the large energy (Fig. 2b). For a typical shock wave in the interplanetary space the magnetic field $B_{shock} = 10^{-4}$ G and the proton energy maximum ~20 GeV, the Larmor radius is $\rho = R/300B \sim 10^{12}$ cm, which is several orders of magnitude higher than the thickness of the observed shock wave. Here R (GV) is the relativistic proton rigidity. Thus, the shock wave in the interplanetary space cannot be a source of the observed relativistic protons after the flare.

According to [2] the proton under certain condition can be captured in the strong magnetic field of a shock wave B_{shock} and gain energy due to the gradient drift, moving along the electric field $E_{shock} = -V_{shock} B_{shock}/c$. The conservation of the proton adiabatic invariant in the shock front is supposed, as shown in Fig. 3, taken from [2]. To explain the acceleration of protons to high energies the authors of [2] consider the possibility of multiple returns of the particles in the acceleration area inside the front due to scattering at magnetic fluctuations. However, such mechanism of proton acceleration also requires the Larmor radius to be smaller than the shock front.

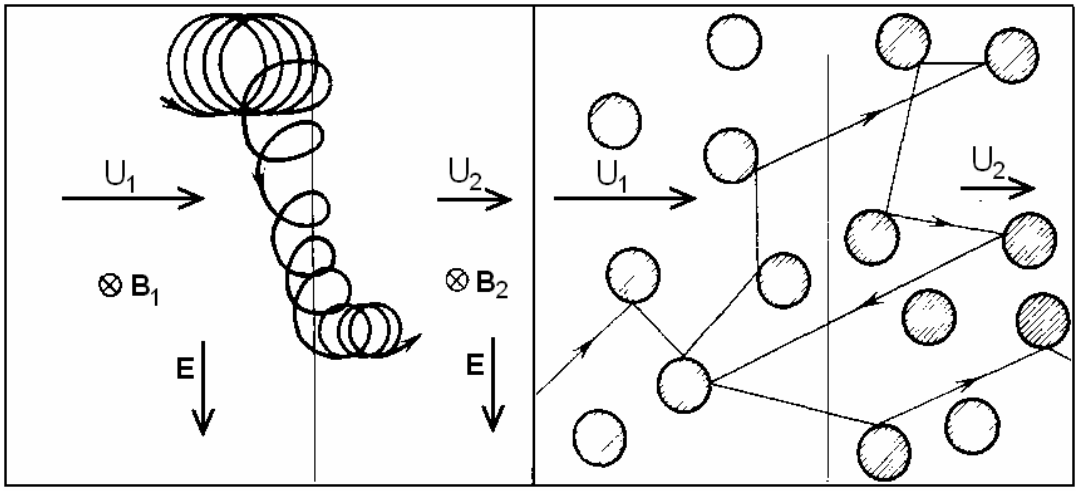

Fig. 3. The drift trajectory of a proton in the shock front. The proton returns inside the front due to scattering on the magnetic field inhomogeneities.

For understanding the mechanism of particle acceleration in a shock front, let us consider the behavior of a particle in the coordinate system associated with the plasma environment in which the particle moves and the shock wave spreads. Two cases are possible:
1. The particle is captured by the front of the shock wave moving in the same direction (Fig. 4a). The particle is decelerated in the Lorentz electric field drifting upward in the area of the magnetic field gradient. The Lorentz electric field is caused by the shock wave movement. The gradient drift is imposed on the drift in the electric field. The resulting drift causes the displacement of the particles along the front. As a result particle acceleration takes place.
2. The particle meets the shock wave front moving to toward (Fig. 4b). The particle is captured in the region of the magnetic field gradient and drifts downward, decelerating in the Lorentz electric field. So, instead of acceleration upon reflection from a magnetic cloud, as shown in figure 2, the gradient drift of the trapped particles leads in such a case to deceleration.

Large fluxes of solar cosmic rays.

Only a part of the X class flares (~30%) and some M class flare accompanied with the great flux $\Phi \geq 1$ cm^{-2} s^{-1} ster^{-1} of relativistic protons are reached the Earth orbit. The spectrum of the proton extends up to 20 GeV [5 - 7]. The average duration of the protons pulse is order of 3 days, while the flare duration, determined from soft and hard x-ray radiation measurements, is order of 20 minutes. The same duration is observed for pulses of γ-radiation (mainly 2.222 MeV) produced by nuclear reactions in the Sun after getting the accelerated protons. That is the duration of the emission of protons is not much different from the flare duration.

Analysis of long-term measurements shows that the parameters of the large relativistic protons flux ($\Phi \geq 1$ cm^{-2} s^{-1} ster^{-1}) reaching the Earth orbit strongly depends on the flare position on the Solar disk. Typical examples of a single emission of large proton fluxes from the Western and Eastern flares are shown in Fig. 5.

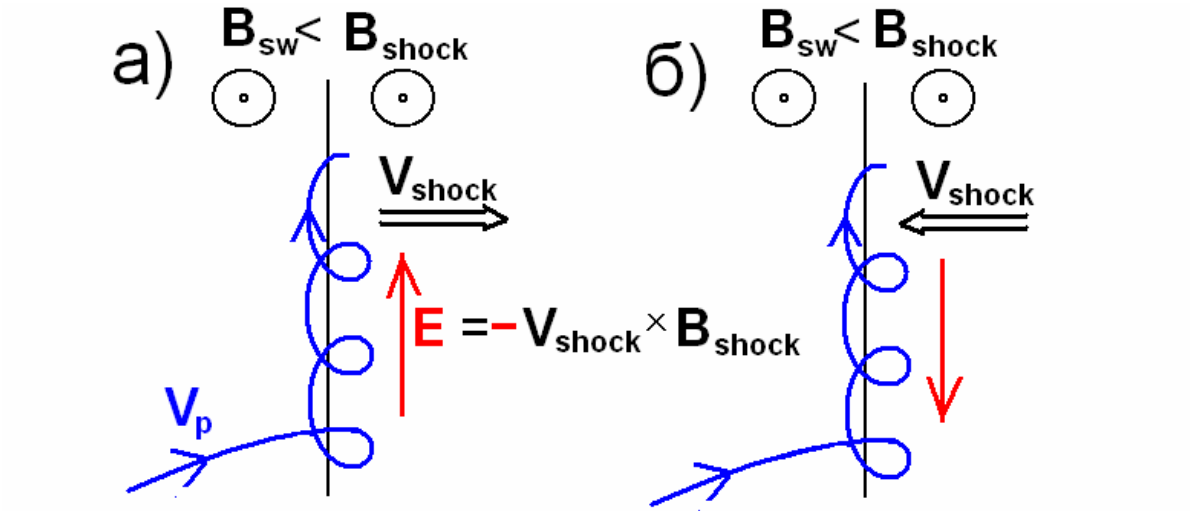

Fig. 4. The trajectory of charged particles entering the shock front. (a) The particle overtakes the shock front. b) The particle moves towards the front.

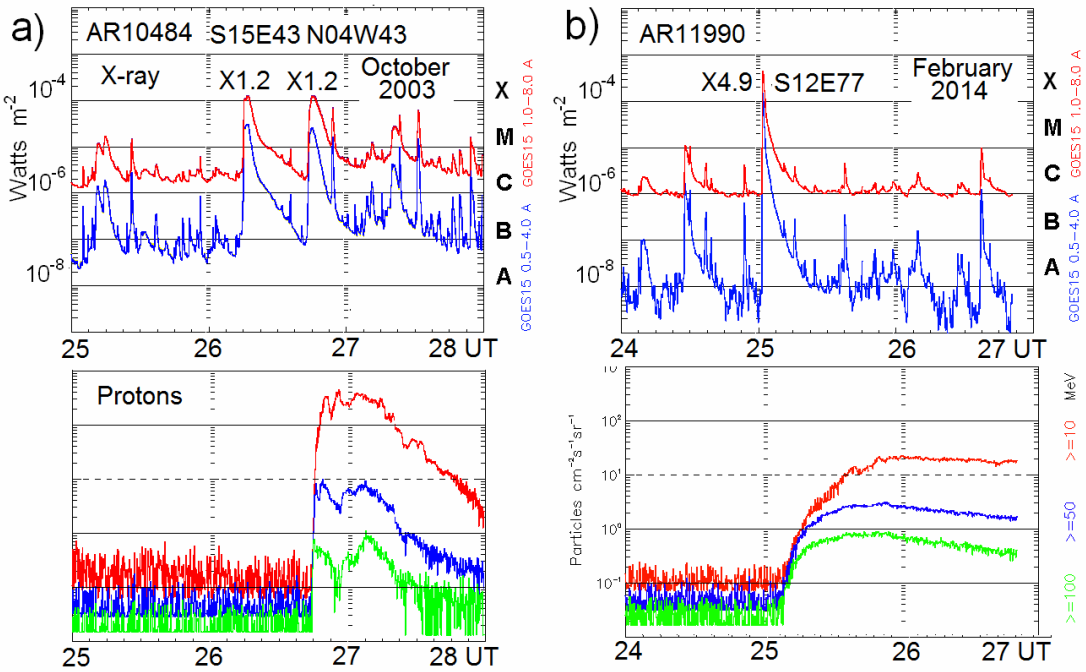

Fig. 5. At the top, a) X-ray emission from the Western proton flare. b) X-ray emission from the Eastern proton flare. Below are the typical large proton fluxes from these flares according to GOES measurements.

The proton flow from a flare that occurred in the West of the Sun has a steep front with duration of about 10 min. The proton flow from this flare comes to the Earth with a delay about 30 min relative to the beginning of the flare. So, the delay is determined by the time of the particle passage from the Sun to the Earth without collisions, apparently along the Arhimed magnetic line. The velocity vector of the particle in the flow front from Western flares is directed, apparently, along magnetic field line. The duration of the proton flow is usually ~3 days. It is equal to the drift time of the protons from the Sun to the Earth with the solar wind velocity (3×10^7 cm/s). At the end of the proton pulse, registered with GOES, particles have arrived that has not been captured by a field line connecting the flare and the Earth. These particles drift across the magnetic field. They propagate in the interplanetary medium with the solar wind velocity. Some particles can arrive earlier, apparently, propagating a part time along a field line, but the other time they drift across the field. The

proton propagation faster than the solar wind could be due to diffusion across the magnetic field at scattering by the magnetic inhomogeneities. In rare cases, the shape of the proton pulse from a Western flare is different from the events shown in Fig. 5a. Sometimes the front of the proton flux is prolonged up to several hours. This happens when the proton flare occurred immediately after other large flares and coronal mass emissions. The helical structure of the interplanetary magnetic field in such a case should be distorted. A unique series consisting of 6 large proton events observed during 10 days from 27.10.2003 on 6.11.2003. Apparently, the interplanetary field was heavily distorted, and the duration the front of the proton flux of the giant Western flare X19 was 10 hours.

Unlike Western proton flares, the protons from Eastern flares and flares that occurred near the central meridian are beginning to register with the delay relative to the beginning of the flare in a few hours. The proton flow front from the Eastern flare is never steep (Fig. 5b). Protons from the Eastern flare are not able to come to the Earth along an Archimed spiral line. They can be transported by the solar wind, and the front can expand by diffusion across the field lines due scattering with the magnetic fluctuations.

Small fluxes of solar cosmic rays.

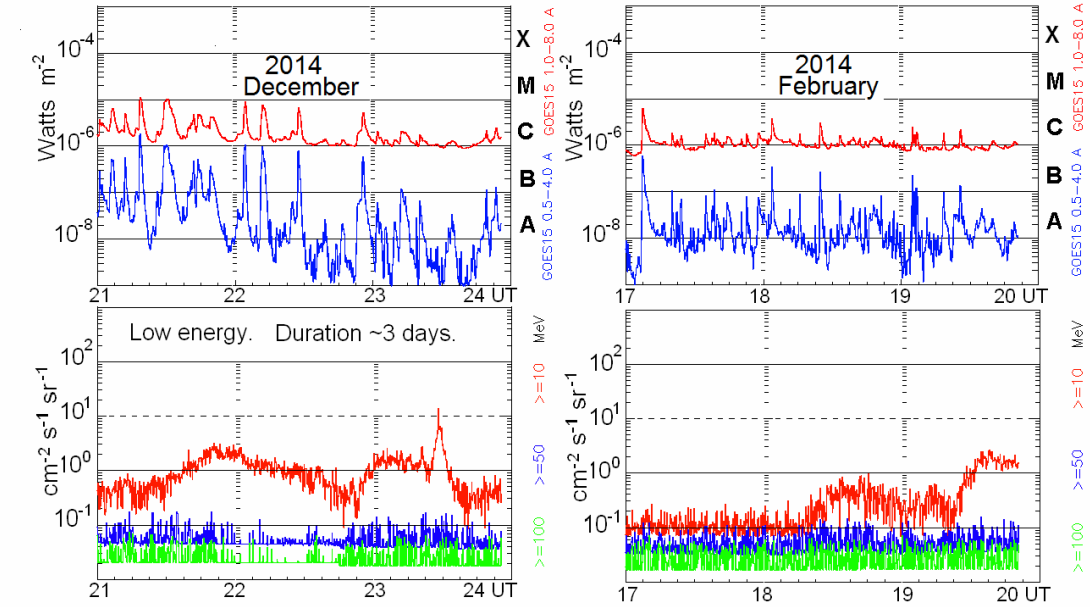

Fig. 6. Above - x-ray emission from flares. Below - a typical small flow of protons according to the GOES measurements.

Small flares ($\Phi \leq 1$ cm^{-2} s^{-1} ster^{-1}) of accelerated protons appear with approximately the same frequency as the large ones ($\Phi \geq 1$ cm^{-2} s^{-1} ster^{-1}). In contrast to the large proton events, the small proton events do not reveal a clear relation to any specific flare. Two examples of small proton events and X-ray pulses of the flares are shown in Fig. 6. Pulses of small proton streams appeared on the background of a number of small flares, mainly of the C class; however, any correlations of proton events with a specific flare are not detected. The duration of small proton events, as the large ones, are observed by days, but their structure is purely individual. No spatial characteristic of small events is observed. The lack of correlation of small proton events with a specific flare observed on the solar disk, apparently, indicates the generation of these events on the back side of the Sun. The protons can arrive along helical magnetic field lines from the night side.

Conclusions.

1. Analysis of the measurement with neutron monitors and GOES suggests that the large proton event is generated by the current sheet during a flare. A clear correlation of small proton events with specific flares is not observed. Apparently, small events are generated by the flares on the back side of the Sun.
2. To accelerate protons in the shock waves it is necessary that the Larmor radius of the particles does not exceed the thickness of the shock front. This condition is impossible in the interplanetary plasma for particles with the energy order of 10 GeV.
3. The proton fluxes of solar cosmic rays reveal four characteristic time scale:
   a). A typical duration of accelerated proton generation is equal to the duration of the flare t_{SF} ~ 20 - 30 min
   b). A typical duration of the accelerated protons flux measured at the Earth orbit is equal to the propagation time of the solar wind t_{SW} = 1a.u./V_{SW} ~ 3 days. This means that the most delayed protons have been captured by the magnetic field of the solar wind and come to the Earth orbit across the magnetic field with the solar wind velocity.
   c). The delay of the steep flux front of relativistic protons generated by the West flare t_F = 15 - 20 min is determined by the time flight of a proton to the Earth orbit along the lines of the Archimedean spiral ~1.5 a.u./c. Collisionless flow of protons along helical magnetic field lines carries information about the spectrum of protons, which according to the neutron monitors data possess the exponential form.
   d). The front of the proton flux from Eastern flares is never being steep. The flux of relativistic protons from the Eastern flare arrives to the Earth with the delay of t_D ~ 3 – 5 hours. The flux increases very slow (~1 day). Such propagation may be associated with the diffusion across the magnetic field lines due to scattering of protons with magnetic inhomogeneities.

Acknowledgments. This work was supported by RFBR grant №13-02-00064.

References

1. Mirishnichenko L.I., Solar Cosmic Rays. *Kluwer. Acad Pabl*., 2001.
2. Berezhko E.G., Krymsky G.F., *Physics-Uspechi.*, **154**, 49 – 90 (1988).
3. Podgorny A.I., Podgorny I.M., *Geomagn. Aeron.*, **52**, 150 – 161 (2012).
4. Podgorny A.I., Podgorny I.M., *Geomagn. Aeron.*, **52**, 162 – 175 (2012).
5. Balabin Yu.V., Vashenuk E.M., Podgorny A.I., Podgorny I.M., *Astron. Reports*, **49**, 837 – 846 (2005).
6. Podgorny I.M., Balabin Yu.V., Vashenuk E.M., Podgorny A.I., *Astron. Reports*, **54**, 645 – 656 (2010).
7. Podgorny I.M., Balabin Yu.V., Podgorny A.I., Vashenyuk E.V., *J. Atm. Solar-Ter. Phys.* **72**, 988 – 991 (2010).

Solar flare model, MHD simulations and comparison with observations

A. I. Podgorny[1], *I. M. Podgorny*[2]

[1] Lebedev Physical Institute RAS, Moscow, Russia,
[2] Institute for Astronomy RAS, Moscow, Russia

Abstract.

The solar flare model is based on the accumulation of magnetic energy in the current sheet, which is formed above an active region. Fast magnetic energy release occurs at the transition of the current sheet in an unstable state. Numerical MHD simulation shows creation of a current sheet in the corona. According to the solar flare electrodynamical model a source of thermal X-ray emission situates in the current sheet. Plasma heating in the sheet occurs due to magnetic energy dissipation. In the numerical simulation no assumptions about the flare mechanism have been done. Due to complexity of the magnetic field, it is necessary to develop the special method of current sheet search in the calculated magnetic field. The method of search is based on the property of the current sheet, according to which the local maximum of the current density is located in the current sheet center. In order to determine whether a given point of the current density maximum corresponds to the current sheet center, the program permits to build the magnetic field configuration. The current sheet is the most clearly presented in the plane, which is perpendicular to magnetic field vector. The search system is used now for study of the solar flares physics. The found current sheet position coincides with the observed position of the X-ray source for the flare 27, 2003 02:53 in the active region NOAA 10365. This coincidence can be considered as a direct indication on the correctness of flare theory based on current sheet creation in the corona.

Introduction. Clarification of the flare mechanism.

It is now established that the solar flare energy is released in the corona above the active regions having a complex distribution of the magnetic field of several kG [1]. Various authors have considered several mechanisms of solar flares production. In [2] is assumed the ejection of the magnetic flux tube with a current (magnetic rope) from the active region, in [3] is examined the possibility of injection of the twisted magnetic field lines (helicity) into the corona and in [4] flare appears due to the sharp change of the current in a magnetic arch above an active region.

All such approaches are based on the assumption of some unstable magnetic configuration existence with the accumulated magnetic energy in the corona or in the chromosphere, which can fast decay heating and accelerating the plasma, and creating beams of high-energy particles. At the same time such approach completely ignores the possibility of the formation of this unstable magnetic system due to observed evolution of the fields and plasma flows in the pre-flare state.

Only the analytical solutions of the MHD equations or the numerical simulation allow us to calculate the magnetic field above an active region and to find out how the energy accumulation for the flare takes place in the corona. To set the initial and boundary conditions it is necessary to use the observed behavior of the active region before the flare. For quick energy release of the accumulated magnetic energy the magnetic configuration must be transferred in an unstable condition and cause flare energy release. The flare mechanism should not be postulates in the numerical experiments, but must be obtained from the results of calculation using real observations in the active region that has produced the flare.

Independently of assumption about the physical mechanism that is responsible for a flare, numerical simulations process should be performed at the initial and boundary conditions taken from the observed state of an active region before a real flare. The flare mechanism should be obtained by simulation results rather than artificially introduced during the setting

of conditions of the numerical simulation. A flare can appear after the magnetic energy ($B^2/8\pi$) accumulation in the magnetic field of a stable configuration, and this energy rapidly dissipates and transfers into the heat and energy of accelerated particles. The process of slow evolution should be replaced by the explosive phase due to instability development.

The criterion of the numerical simulation correctness of pre-flare state of the magnetic field and the plasma above the active region is simple: dissipation of the stored magnetic energy after the development of the instability should provide the main flare manifestations:

1. The energy release over the active region, which is registered by RHESSI measuring the thermal x-ray emission of the dense plasma above an active region.
2. The acceleration of electron beams precipitating on the surface of the Sun, which is registered by the hard x-ray radiation.
3. The creation of the fast plasma flow into the interplanetary space (CME).
4. Generation of relativistic protons.

The modern developed methods for numerical solution of the MHD equations allow determining the magnetic field distribution above the active region before the flare, i.e. to find out what is the configuration of the magnetic field that provides the magnetic energy accumulation for a real flare. The matching thus obtained configuration fields with the results of flare observation, performed by various methods, make it possible to build a model of the flare, without introducing any artificial assumptions about flare nature.

In the present work for the first time we determine the magnetic field configuration before the flare above the active region using only data from the photospheric measurements. No assumptions about the mechanism of energy storage are introduced. It is shown that energy accumulation occurs in the current sheet magnetic field. Current sheet decay in the corona must produce the development of the main processes observed in the flare. The flare development can be described by electrodynamical model of the solar flare.

Methods and conditions of MHD simulation

Simulations [5] show, that to take into account all singularities of magnetic field configuration, it is necessary to perform MHD simulations in the numerical domain which size is several times bigger then the size of active region. The simulations for AR 0365 have been done in domain with the size 4×10^{10} cm. The simulations have been started several days before the series of flares 27 May 2003 produced by AR 0365. In this time the strong disturbances in corona were absent, and the potential magnetic field can be taken for setting the initial conditions. To find potential magnetic field the Laplace equation is solved numerically with oblique derivative boundary conditions on the photosphere. The distributions of the line-of-sight magnetic field component are taken from magnetic maps observed by SOHO MDI (http://soi.stanford.edu/magnetic/index5.html) for setting photospheric boundary conditions. Others boundary conditions are approximated by free-exit conditions.

The simulations are performed by numerical solving of 3D MHD equations above the active region in the solar corona. Its lower boundary is situated on the photosphere and contains the active region AR 0365. The calculations are done in the computational domain ($0\le x\le 1$, $0\le y\le 0.3$, $0\le z\le 1$, in dimensionless units). The unit of the length is chosen as the size of photospheric boundary of the computational domain $L_0=4\times10^{10}$ cm. The Y-axis is directed away from the Sun normally to the photosphere. The XZ (y=0) plane is the photospheric plane. The X-axis is directed from East to West, and the Z-axis is directed from North to South. Situation of photospheric boundary of the computational domain ($y=0$, $0\le x\le 1$, $0\le z\le 1$) in the flare day 27 May 2003 is shown in Figure 1a. The magnetic field $B_0=300$ Gauss is taken as a unit. The dimensionless units of the plasma density ρ_0 and the temperature T_0 are taken to be equal to their values in the initial moment of time in the corona, which are

supposed to be constant in space. $n_0=10^8$ cm^{-3} ($\rho_0=n_0 m_i$, m_i is the ion mass), $T_0=10^6$ ^oK. The dimensionless units of the plasma velocity, time, and the current density are taken as correspondingly the Alfven velocity $V_0 = V_A = B_0 / \sqrt{4\pi\rho_0}$, $t_0 = L_0/V_0$, $j_0 = cB_0/4\pi L_0$. The 3D dimensionless MHD equations have the form:

$$\frac{\partial \mathbf{B}}{\partial t} = \mathrm{rot}(\mathbf{V}\times\mathbf{B}) - \frac{1}{\mathrm{Re}_m}\mathrm{rot}\left(\frac{\sigma_0}{\sigma}\mathrm{rot}\mathbf{B}\right) \quad (1)$$

$$\frac{\partial \rho}{\partial t} = -\mathrm{div}(\mathbf{V}\rho) \quad (2)$$

$$\frac{\partial \mathbf{V}}{\partial t} = -(\mathbf{V},\nabla)\mathbf{V} - \frac{\beta_0}{2\rho}\nabla(\rho T) - \frac{1}{\rho}\left(\mathbf{B}\times\mathrm{rot}\mathbf{B}\right) + \frac{1}{\mathrm{Re}\rho}\Delta\mathbf{V} + G_g\mathbf{G} \quad (3)$$

$$\frac{\partial T}{\partial t} = -(\mathbf{V},\nabla)T - (\gamma-1)T\mathrm{div}\mathbf{V} + (\gamma-1)\frac{2\sigma_0}{\mathrm{Re}_m\sigma\beta_0\rho}\left(\mathrm{rot}\mathbf{B}\right)^2 - (\gamma-1)G_q\rho L'(T) +$$

$$+\frac{\gamma-1}{\rho}\mathrm{div}\left(\mathbf{e}_{\|}\kappa_{dl}(\mathbf{e}_{\|},\nabla T) + \mathbf{e}_{\perp 1}\kappa_{\perp dl}(\mathbf{e}_{\perp 1},\nabla T) + \mathbf{e}_{\perp 2}\kappa_{\perp dl}(\mathbf{e}_{\perp 2},\nabla T)\right) \quad (4)$$

The restrictions connected with the finite step of the difference scheme do not permit to set real dimensionless parameters, which characterize the diffusion terms of equations (1)-(4). The principle of limited simulation [6] is used. According to this principle, the dimensionless parameters, which are much larger then 1 should be chosen larger than 1 in the numerical experiment, but their order of magnitude can be different. In our calculations the parameters are chosen as $\gamma = 5/3$, $\mathrm{Re}_m=1000$, $\mathrm{Re}=300$, $\beta=0.6\times10^{-5}$, $\Pi=100$, $\Pi_B=10^4$, $G_q=0.3\times10^{-5}$. The gravitation force can be neglected comparing with magnetic and plasma pressure forces: $G_g=0$.

To stabilize the numerical instabilities it is used an absolutely implicit finite-difference scheme, which is solved by the iteration method [7]. The scheme is also conservative relative to the magnetic flux. The artificial viscosity is introduced near the computational domain boundary, and some other special methods are used.

The numerical solving of MHD equations is initiated three days before the flare, when there are no strong disturbances and the magnetic field in the active region of the solar corona can be considered as potential one. The potential magnetic field is found by solving of the Laplace equation for the magnetic potential φ_B ($\mathbf{B}= -\nabla\varphi_B$) with the tilted derivative along the line-of-sight as the boundary condition on the photospheric boundary:

$$\Delta\varphi=0; \quad \partial\varphi/\partial l_{\mathrm{sight}}|_{\mathrm{PhBoun}}=-B_{\mathrm{lsight}}; \quad \mathbf{B}=-\nabla\varphi \quad (5)$$

The distribution of the line-of-sight magnetic field component B_{lsight} on the photosphere is taken from magnetic maps obtained by SOHO MDI (http://soi.stanford.edu/magnetic/index5.html). The special methods are developed to obtain the potential field in such approximation to be stable solution of MHD equations system for using finite-difference scheme which is absolutely implicit and conservative relative to magnetic flux. The Laplace equation (5) is solved using a finite-difference scheme on the same grid as for solving MHD equations (1-5). To minimize $|[\mathrm{div}\mathbf{B}]|$ after solving of the Laplace equation for the field potential with tilted derivative as boundary condition (see [5]). It is done two corrections of field. The first of them is solving of the diffusion equation for $\mathbf{B}$ $\frac{\partial \mathbf{B}}{\partial t} = \Delta\mathbf{B}$ with the scheme (1). The second one is inserting magnetic charges in the center of cells of the numerical greed with the value $q=-[\mathrm{div}\mathbf{B}]V_{\mathrm{cell}}/4\pi$ (V_{cell} is the cell volume).

For solving the equation (5), it is necessary to set condition on the nonphotospheric boundary. Here the magnetic field is small, and it can not produce any strong influence on the solution inside the region. The conditions on nonphotospheric boundary are set by two methods. According to the first one, the normal component on the nonphotospheric boundary

$B_{NoPhBoun}$ is set as a constant. $B_{NoPhBoun}$ is calculated from the condition that the full magnetic flux through the boundary of calculation region is equal to zero (the outgoing flux is equal to the flux directed inside the region). For Laplace equation (5) solving the condition $\partial\varphi/\partial n=-B_{NoPhBoun}$ is set on nonphotospheric boundary. According to the second method, the potential φ is set to be zero on the nonphotospheric boundary. The results obtained by the both methods are almost the same.

To solve the system of MHD equations it is need to set two magnetic field components parallel to the boundary on the photospheric boundary of the domain in each moment of time. But SOHO MDI observes on the photosphere only the line-of-sight magnetic field component. For setting boundary conditions, two parallel to the photosphere magnetic field components are taken from calculated potential magnetic field by solving of the equation (5) by the same way as for the initial moment of time. Such method is valid because the magnetic field on the photosphere is defined mainly by the currents under the photosphere, but not by the currents in the corona.

The dimensionless initial conditions for the density, temperature, and velocity take the form:

$$\rho=1;\ T=1;\ V_x=0;\ V_y=0;\ V_z=0$$

The plasma density, velocity, and temperature at the photospheric boundary are specified as follows:

$$\rho=1,\ \partial V_x/\partial n=0,\ \partial V_y/\partial n=0,\ \partial V_z/\partial n=0,\ \partial T/\partial n=0$$

At the other boundaries, these conditions take the form

$$\partial\rho/\partial n=0,\ \partial V_x/\partial n=0,\ \partial V_y/\partial n=0,\ \partial V_z/\partial n=0,\ \partial T/\partial n=0$$

The change of the photospheric magnetic field leads to evolution of the coronal magnetic configuration that simulated by solving MHD equations. In spite of special methods used to stabilize numerical instability it is necessary to have sufficient small time step, otherwise a numerical instability appears. Therefore, the equations are solved slowly, and computations were performed on a time scale shortened by four orders of magnitude in order to accomplish this procedure using the available computer. The calculations performed on a shortened time scale made it possible to understand the general pattern of the magnetic field behavior above an active region and to find the current sheet positions, which appear in the places of X-type singular lines.

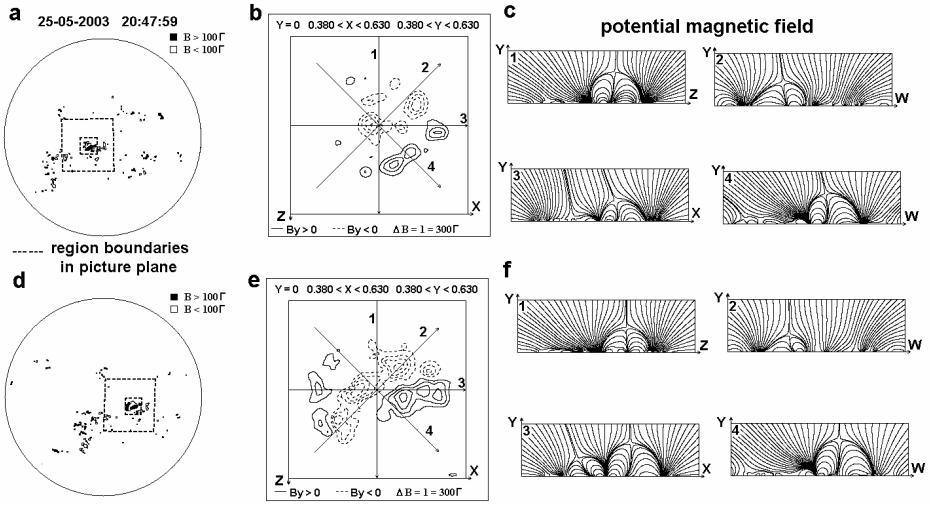

Figure 1. (a, d) SOHO MDI magnetic maps on the solar disk on May 25 and 27, 2003. The positions of the L0=4×1010 and L0=1.2×1010 domains are demonstrated. (b, e) The contour lines of the magnetic field normal component in the active region; (c, f) the configurations of the potential magnetic field in the planes perpendicular to the photosphere; the projections of planes 1–4 are shown in (b) and (e).

Results of MHD simulation in the solar corona above the active region: the current sheet appearance and development

The initial potential magnetic field configuration above the active region AR 10365 is presented in Figure 1 in planes perpendicular to photosphere, which cross the photosphere by lines shown in the Figures 1b, 1e. In each plane the X-type magnetic field configuration is presented, which means that somewhere near it the X-type singular line must be situated. In the vicinity of this X-type singular line the current sheet can be created by focusing of disturbances. The disturbances are propagated from the photosphere. In MHD simulation such disturbances appears due to setting of observed magnetic field, which change in time, on the photosphere boundary.

The Figure 2 demonstrates that numerical MHD simulation shows the current sheet appearance. The left panels present the distribution contours of the magnetic field component, which is normal to the photosphere in the active region; 1–4 show the intersections of the corresponding planes with the photosphere. In each plane perpendicular to the photosphere the magnetic field near to the X-point deforms into configurations, which remind current sheet. The positions of such current sheet configurations are shown by arrows. It does not mean that we see the current sheet in this place of the plane, because the X-type magnetic singular line can be inclined at some angle to this plane. But it means that the current sheet appears in the vicinity of X-type singular line near the place of field deformation in the plane. Our purpose is to find the current sheet and its magnetic field configuration, which is most distinctly pronounced in the plane perpendicular to the singular line.

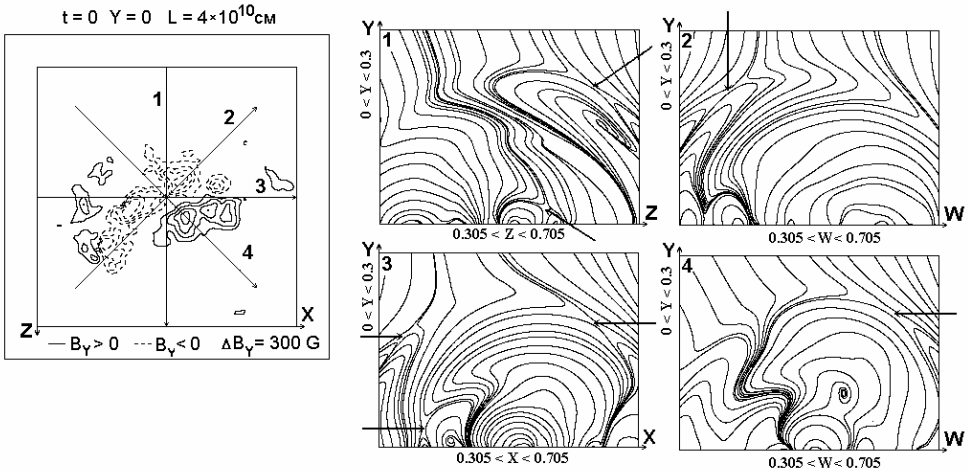

Figure 2. Calculated magnetic field configuration in the corona above AR 10365 before a series of flares in the planes perpendicular to the photosphere. The position of the planes is shown on the left-hand side. The arrows mark the produced current sheets.

A numerical simulation of a current sheet [8, 9] indicated that the plasma density near the sheet decreases during a quasistationary evolution process. The decrease of the plasma density results in an instability and explosive energy release [10, 11].

The calculated magnetic field configurations [5] in the most representative central plane of the region show appearance of several current sheets (see Figure 3). The disturbances that originated on the photosphere propagate upward into the corona. The magnetic field is deformed in the vicinity of the X points (arrows 1 and 2) that existed in the potential magnetic field at the instant t= 0, and current sheets are formed. By the t= 2.2 instant, the current sheets marked by arrows 1 and 2 are formed, and a sheet originates near the photosphere (marked by arrow 3). The field lines of sheets 2and 3are scaled up in the bottom panels. The field configuration corresponds to typical current sheets with the normal component of the magnetic field. As the magnetic field emerges, the current sheets move upward, and the sheet

2 goes beyond the computational domain by instant 3.8. The field lines of this current sheet are located so that it is difficult to detect this sheet in the Z= 0.5 plane.

Figure 4 shows the field lines in the three-dimensional space near the horizontally located sheet marked by arrow 2. These data correspond to the field configuration that originated on May 26, 2003.

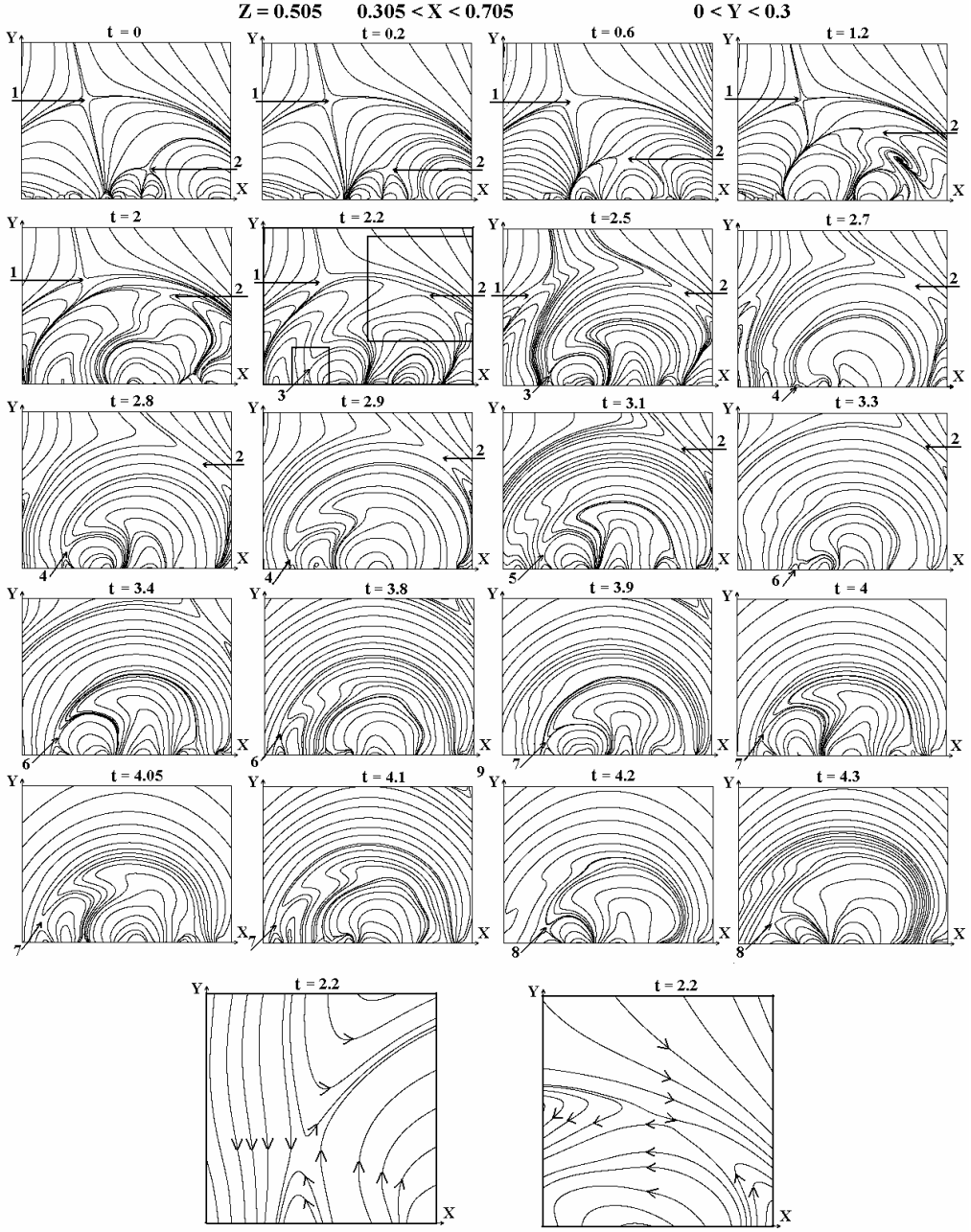

Figure 3. Magnetic field lines in the central plane of computational domain in corona above the active region obtained by MHD simulations. The current sheets are indicated by arrows. Below, the field lines near the two current sheets indicated by arrows 2 and 3 for time t = 2.2 are shown on an expanded scale.

To find positions of sources of soft X-ray radiation in the corona the graphical system developed by authors is used. The current sheet property is used, according to which the local maximum of the absolute value of the current density is located in the center of a current sheet. In any selected plane, which can be placed arbitrarily in the space in the computational domain, the lines of level of absolute values of current density are constructed. Furthermore, in this plane all positions of the local current density maxima in the plane and projections on

the plane of all positions of the local maxima of the current density in the space are marked. Marked points are located at the intersection of the current sheets with the plane, or they are corresponded to current sheets centers. The program can easily obtain information about any marked point of the maximum. It can be outputted coordinate value of that point in any chosen coordinate system and the all calculated values (magnetic field vector, plasma density, and plasma temperature, etc.) in this point. In order to determine whether a given point of the current density maximum corresponds to the current sheet center or simply corresponds to an increase of the current density as a result of some disturbance, the program offers the possibility to build the magnetic field configuration in the vicinity of the selected point in any arbitrarily rotated coordinate system. Typically, in first turn it is expected to build the magnetic field configuration in a plane containing the selected point of the current density maximum which is situated perpendicular to the magnetic field vector. [12].

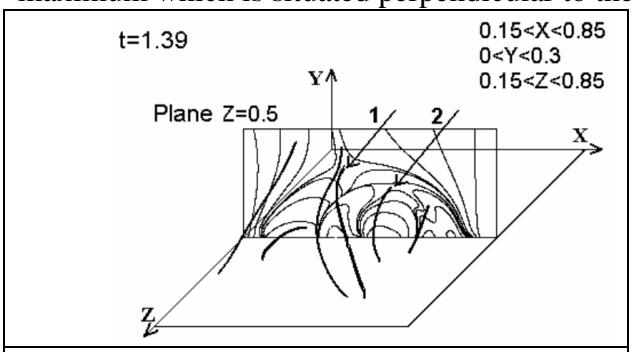

FIGURE 4. MAGNETIC FIELD CHARACTERISTIC LINES IN THREE DIMENSIONAL SPACE (THICK LINES) AND ON THEZ= 0.5 PLANE.

The developed graphical system permits to find of the current sheet position for the flare, which occurred May 27, 2003 at 02:53 above the active region NOAA 10365. The coordinates of the center of the founded current sheet in the computational domain are (0.46, 0.04, 0.445). It situated on the height ~ 16 000 km. Taking into account that on such small height the magnetic field is large, the position of a such current sheet, must correspond to the solar flare place. In the vicinity of this local maximum in the plane, which is perpendicular to the magnetic field vector, the magnetic field configuration corresponds to the pronounced current sheet distinctly (see Figure 5a) The lines of equal current density in this plane and 3D magnetic lines are presented in Figures 5 b, c.

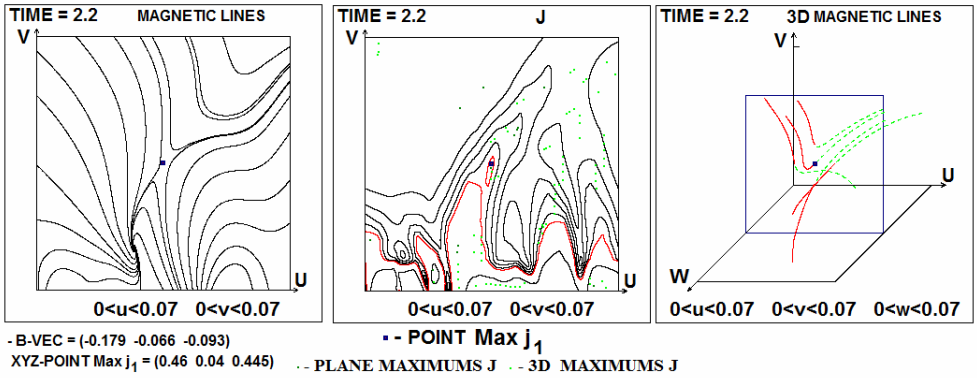

Figure 5. a, b – Magnetic field configuration and lines of equal current density in the plane which contains the point of current density maximum with coordinates (0.445, 0.105, 0.42) and which is situated perpendicular to magnetic field vector B=(0.0086, 0.0264, 0.0819). The 3D magnetic lines are presented in the left panel, behind the plane they are marked as dashed lines.

The current sheet position coincides with the position of the source of thermal X-ray. [13]. This coincidence is independent evidence of the solar flare mechanism, based on the accumulation of the flare energy in the current sheet magnetic field in the corona.

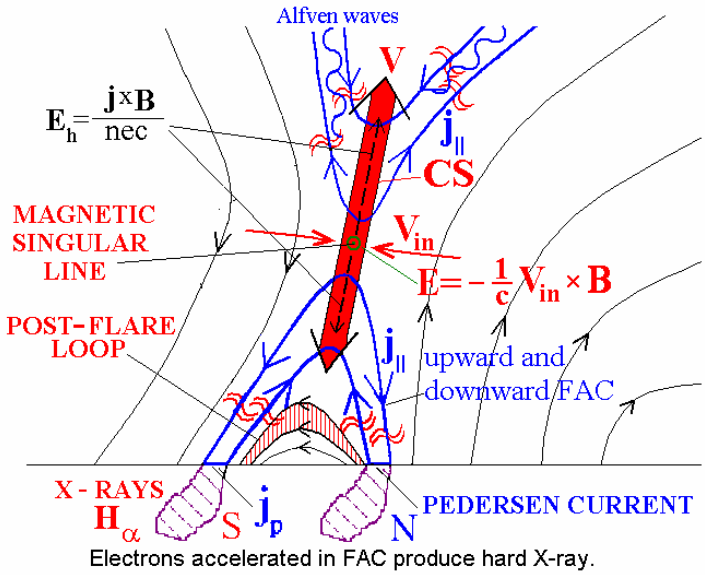

Figure 6. The electrodynamic model of the flare. The magnetic field lines are shown by thin lines and arrows; the field-aligned currents are demonstrated by thick lines and arrows.

Conclusion. Solar flare model

Numerical simulation permits to conclude that energy accumulation for the solar flare takes place in the current sheet magnetic field. Decay of this current sheet should cause the complex of phenomena detected during the flare. The most informative data were obtained in the measurements of X-ray emission on the spacecraft RHESSI. The position of the thermal X-ray emission source coincides with the calculated position of the current sheet. Thus, it can be concluded that the fact of plasma heating by dissipation of the current sheet magnetic field is established. The measurements in the magnetospheric tail and laboratory experiments [14] show generation of the Hall electric field j×B/nec in the current sheet. The Hall field should produce field-aligned currents, in which the electrons must be accelerated and precipitate on the solar surface. The source of hard beam X-ray emission is registered on the solar surface by RHESSI. The numerical simulation [15] shows proton acceleration up to relativistic energies by electric field along the singular line of the current sheet. The **j×B** force should accelerate the plasma along the sheet, and eject it into space (Coronal mass ejection). Matching of these observational data and the fact of current sheet creation before the flare, obtained by numerical simulation, permits us to propose the electrodynamic model of the flare, shown in Figure 6. The model explains release of the magnetic energy accumulated above the active region and the main observational manifestations of the solar flare.

Acknowledgments. This work was supported by RFBR grant №13-02-00064.

References.

1. Podgorny I.M., Podgorny A.I., Meshalkina N.S., *Sun and Geosphere*. **8**, 63 – 69 (2013).
2 Kliem B., Titov V.S., Torok T., *Astron. Astrophys. 413*, L23-L26 2004.
3.Kusano, K., Yokoyama T., Maeshiroi T., Sakurai T., *Adv. Space Res.*, **32**, 1931 – 1936 (2003).
4. Zaitsev V.V., Stepanov A.V., *Progress in Physical Science (Physics Uspekhi)* 178, 1166 – 1197 (2008).
5. Podgorny A.I, Podgorny I.M., *Astronomy Repoprts*. 52, 666 – 675 (2008).
6. Podgorny I.M., *Fund. Cosmic Phys.* **1**, 1 – 72 (1978).
7. Podgorny A. I., Podgorny I. M. *Comput. Mathematics and Mathemat. Physics*. **44**, 1784 – 1806 (2004).
8. Bilenko I.A., Podgorny A.I., Podgorny I.M., *Solar Phys.* **207**, 323 – 336 (2002).
9. Podgorny A.I, Podgorny I.M., *Astronomy Repoprts*. 47, 696 – 702 (2008).
10. Podgorny A.I. *Solar Phys.* **123**, 285 – 308. (1989).
11. Podgorny A.I. *Plasma Physics and Controlled Fusion.* **31**, 1271 – 1279 (1989).
12. Podgorny A.I., Podgorny I.M, Meshalkina N.S., *Solar System Research*. **41**, 322 – 329 (2007).
13 Podgorny A.I., Podgorny I. M., *Sun and Geosphere.* **8**, 71 – 76 (2013).
14 Minami S., Podgorny A.I., Podgorny I.M., *Geophys. Res. Letts.* **20**, 9 – 12 (1993).
15 Podgorny I.M., Balabin Yu,V., Podgorny A.I., Vashenyuk E.V., *J. Atm. Solar-Ter. Phys.* 72, 988 – 991 (2010).

CME in the interplanetary medium by observations of IPS at the decameter wavelengths

N.N. Kalinichenko[1], *A.A. Konovalenko*[1], *A.I.Brazhenko*[2], *V.V. Solov'ev*[1]
[1] Institute of radio astronomy, Kharkiv, Ukraine
[2] Gravimetric observatory, Poltava, Ukraine
E-mail: kalinich@rian.kharkov.ua

INTRODUCTION

We carry out interplanetary scintillation (IPS) observations of cosmic radio sources (Hewish et al. 1964) with using URAN decameter radio telescope system (8 - 32 MHz, Ukraine). During the last few years the registration, control and others systems of the radio telescopes composing URAN system (UTR-2, Grakovo; URAN-1, Zmiyov; URAN-2, Poltava; URAN-3, Lviv; URAN-4, Odesa) were essentially improved. These improvements and the development of the new effective methods for weakening ionospheric and interference effects allow us to raise efficiency of IPS observations and experimental data reliability. Among other these allow us to find and to study large scale moving disturbances in the solar wind associated with coronal mass ejections (CME). In particular, we manage to find and to study the large scale disturbance in the solar wind associated with Valentine's day CME (15 February 2011).

At present time investigations of coronal mass ejections in the interplanetary medium (ICME) with using IPS observations at high frequencies (more or about 100 MHz) are common at the distances from the Sun less than 1 a. u. We manage to observe ICME at the distances from the Sun, which is more than 1 a. u., by observing IPS at decameter wavelengths at solar elongations (angle between the directions to the Sun and the source) more than 90^o. This became possible, as at the decameter wavelengths the cosmic radio sources show good scintillations right up to elongations of about 180^o, at which the high frequencies (more or about 100 MHz) are only slightly scattered by low density plasma at the large distances from the Sun (large solar elongations correspond to large distances from the Sun).

OBSERVATIONS

Valentine's day CME took place in February 15, 2011, about 01:57 UT and was registered by SOHO and Stereo A, B spacecrafts. SOHO, Stereo A, B spacecraft data showed that Valentine's day CME was an Earth-directed, had an initial speed of about 1000 km/s and was expected to reach the Earth on late 17^{th} to early 18^{th} February 2011 (Lee et al. 2013). The angular width of CME was $65–85^o$.

Observations of IPS were synchronously made with the largest in the world decameter radio telescope UTR-2, Grakovo (Braude et al. 1978) and the decameter radio telescope URAN-2, Poltava (Megn et al 2003). Every day, from February 16 to February 22,2011, three radio sources (3C144, 3C196 and 3C273) were observed at elongations of 114^o, 136^o, 143^o, correspondingly. Records were obtained by using digital spectrum analyzers DSP-z (Ryabov et al. 2010) with parameters of registration: the continuous frequency range - 20.63 to 28.88 MHz, the time constant - 20 ms. The use of the digital spectrum analyzers and records from two radio telescopes allows us to apply special methods for weakening ionospheric and interference effects and to achieve sensitivity that is close to maximal. Figures 1 a - d show examples of data recordings for February 17, the day before ICME came to the Earth (Figure 1 a, b) and February 18, the day when ICME crossed Earth's orbit and appeared on the lines of sight to the observed radio sources (Figure 1 c, d). The difference in scintillation levels for these two days is visible to the unaided eye.

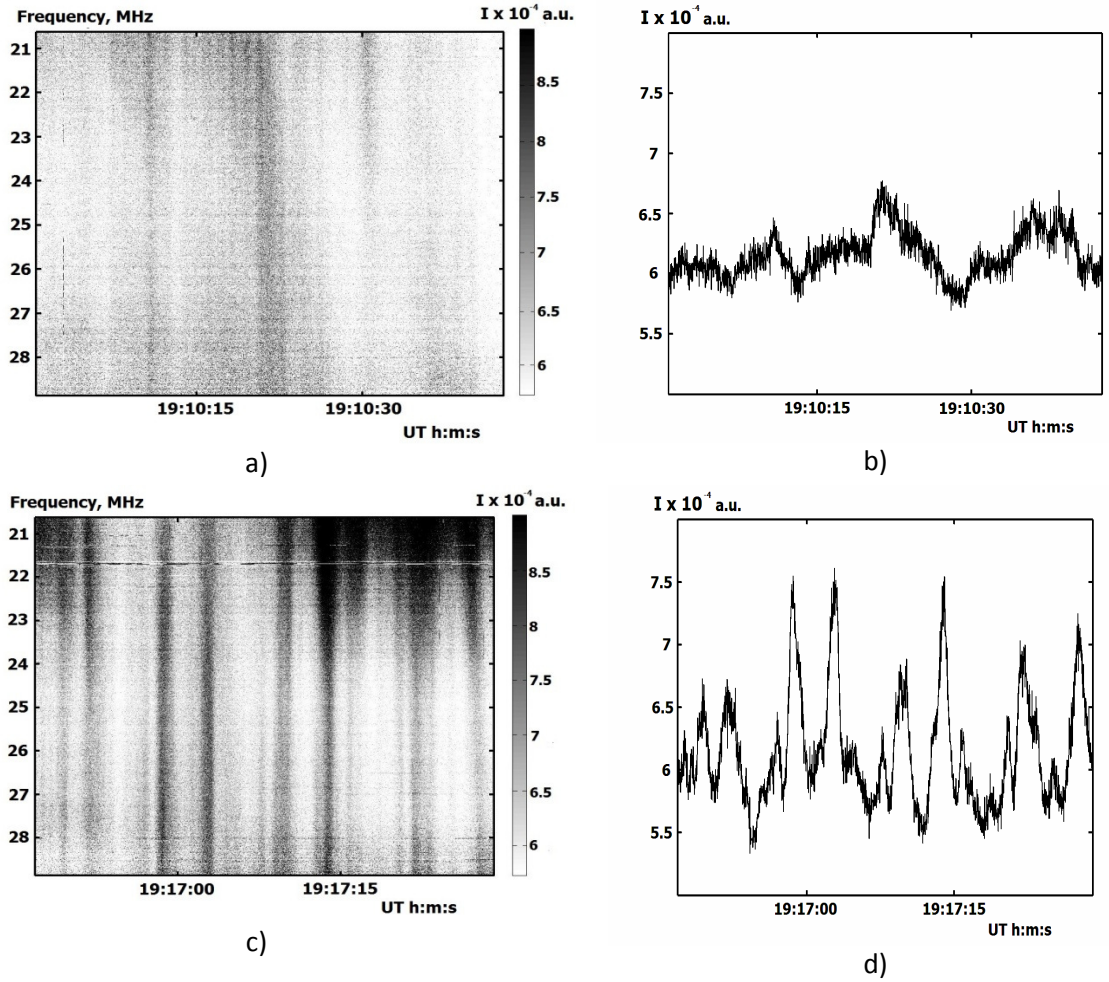

Figure 1. Two examples of data recordings for February 17 (a, b) and February 18 (c, d). a) and c) are dynamic spectra (intensity in arbitrary units on the frequency vs time plane). b) and d) are the sections of the corresponding dynamic spectra at the frequency of 25 MHz.

DATA PROCESSING

Data processing consists in estimation of power spectrum $P(\nu)$ and scintillation index m for all radio sources and for all days of observations. $P(\nu)$ is defined by

$$P(\nu) = |F(\nu)|^2 / T,$$

where $F(\nu)$ is Fourier transform of $I(t)$ process, ν is the fluctuation frequency, T is the duration of time series.

Scintillation index m is determined from formula

$$m = \frac{\sigma_{IPS}}{\overline{I(t)}} = \frac{\sqrt{\sigma^2_{(IPS+n)} - \sigma^2_n}}{\overline{I(t)}} \quad ,$$

where $\overline{I(t)}$ is the mean intensity of the radio source, σ^2_{IPS}, σ^2_n, $\sigma^2_{(IPS+n)}$ - are the dispersions of the interplanetary scintillations, noise and their sum estimated from the power spectrum.

DATA ANALYSES

Figure 2 shows the averaged power spectra which were estimated for 5 observational days (radio source 3C144, Crab Nebula). It is clearly seen the difference of the cutoff frequency for each spectrum. For February 18, 19 and 20 the cutoff frequencies are equal to 0.3, 0.15 and 0.12, correspondingly.

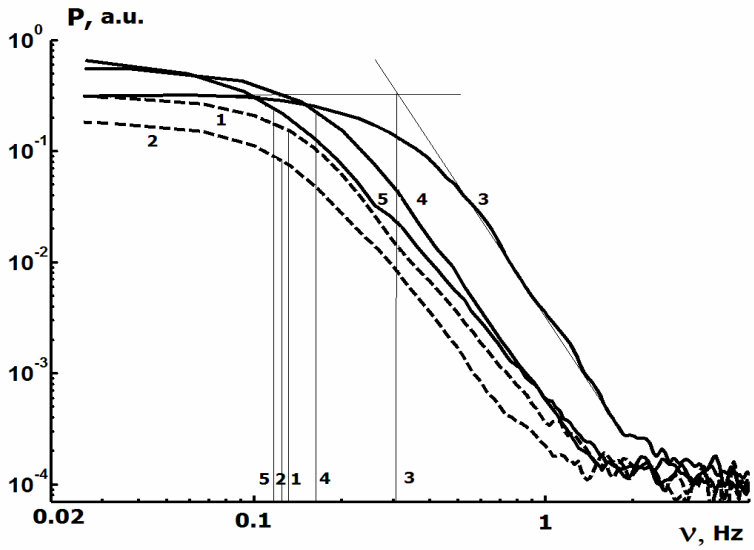

Figure 2. Power spectra for radio source 3C144: 1 - 16.02.2011, 2 - 17.02.2011, 3 - 18.02.2011, 4 - 19.02.2011, 5 - 20.02.2011

The behaviour of the scintillation index during the corresponding days for observed radio sources is demonstrated in Figure 3. The abrupt increase of the scintillation index on late 18^{th} to early 19^{th} February 2011 is connected with the appearance of ICME on the lines of sight to the observed radio sources.

Knowledge of the cutoff frequency allows conclusions to be made on the distance to the scattering layer using simple formulas (phase screen model):

$$\nu_{cutoff} = \frac{V_{\perp}}{\sqrt{2\pi\lambda z}},$$

from which the distance to the scattering layer can be defined by

$$z = \frac{V_{\perp}^2}{2\pi\lambda\nu_{Френ}^2}$$

For 3C144 the distance z is equal to 0.2, 0.6. and 1.0 a. u. for February 18, 19 and 20, correspondingly. For 3C273 the distance z equals 0.1, 0.4 and 0.7 a. u. The position of CME in the interplanetary medium beyond Earth's orbit can be reconstructed by using data from all radio sources and accepting cone model of CME (Lee et al. 2013) (see Figure 4).

Analyses of all data allows the following conclusions to be made.

CONCLUSIONS

The carried out investigations showed the high efficiency of the interplanetary scintillation method in the decameter range of radio waves for discovering and studing ICME beyond Earth's orbit. It is established that coronal mass ejection in the interplanetary medium continues slowing at distances from 1 to 1.7 au from the Sun, its velocity tending to the velocity of the ambient solar wind, the angular size being not less than 66^0.

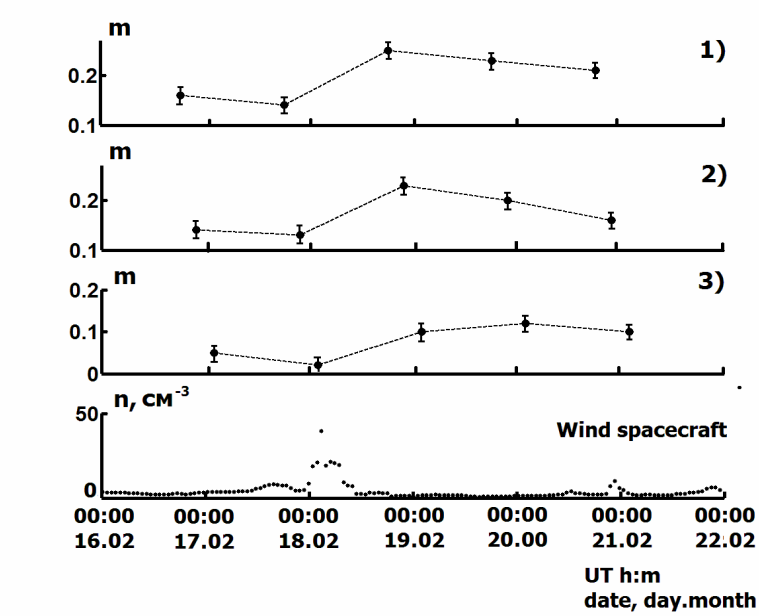

Figure 3. The behaviour of the scintillation index during the corresponding days for observed radio sources (1 - 3C144, 2 - 3C196, 3 - 3C273) and the proton density in the solar wind measured by NASA spacecraft Wind (the bottommost panel of the Figure)

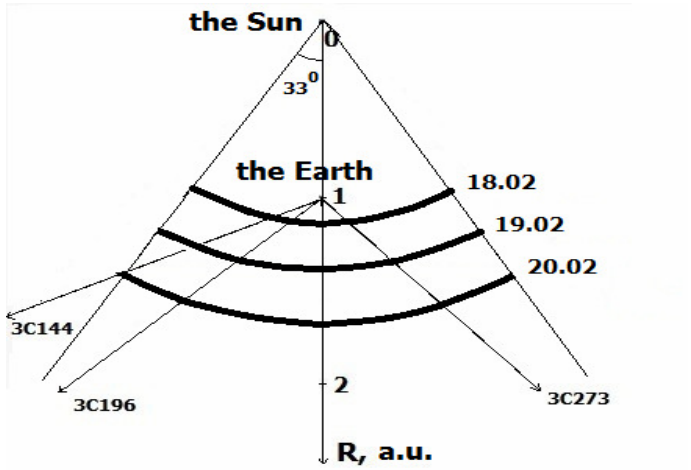

Figure 4. The position of CME in the interplanetary medium beyond Earth's orbit for February 18, 19 and 20, 2011.

REFERENCES

Braude, S.J., Megn, A.V., Sodin, L.G. 1978, in A.Pistolkors (ed.), Antennas, 26, 3.

Hewish, A., Scott, P.F., Wills, D. // Nature. -1964. -Vol. 203, 1214.

Lee C.O., Arge C.N., Odstrcil D., Millward G., Pizzo V., Quinn J.M., Henney C.J. Ensemble modeling of CME propagation. // Solar physics. -2013.-Vol. 285, Issue 1. - P. 349-368.

Megn A.V., Sharykin N.K., Zakharenko V.V., Bulatsen V.G. Brazhenko A.I. Vashishin R.V. Decameter radio telescope URAN-2 // Radiofizika i radioastronomia. -2003. - V. 8, N 4. - P. 345 -356.

Ryabov V.B. Vavriv D.M., Zarka P. A low-noise, high-dynamic-range, digital receiver for radio astronomy applications: an efficient solution for observing radio-bursts from Jupiter, the Sun, pulsars, and other astrophysical plasmas below 30 MHz // Astron. Astrophys. - 2010. - Vol. 510. – P. 13.

CMEs and frequency cut-off of solar bursts

Aleksander Stanislavsky, Aleksander Konovalenko, Artem Koval, Yaroslav Volvach

Institute of Radio Astronomy, 4 Chervonopraporna Str., Kharkiv 61002, Ukraine
E-mail: astex@ukr.ua

ABSTRACT

Observations of solar bursts with high-frequency cutoff by the radio telescope UTR-2 (near Kharkiv, Ukraine) at 8-33 MHz on 17-19 August 2012 are presented. Such cut-off may be attributed to the emergence of the burst sources behind limb of the Sun toward the Earth. The events are strongly associated with solar eruptions occurred in a new active region. Ray tracing calculations show that the CMEs play a constructive role for the behind-limb bursts to be detected in ground-based observations. Likely, due to tunnel-like cavities with low density in CMEs, the radio emission of solar bursts is directed to the Earth.

INTRODUCTION

Coronal mass ejections (CMEs) tightly are associated with three types of low-frequency radio bursts [1], namely II, III and IV types. The bursts mirror the processes that initiate and develop phenomena accompanying CMEs. In particular, the source of type III bursts is accelerated electrons propagating along open magnetic field lines, whereas type II bursts are emitted by electrons accelerated in shocks. Consequently, each type of the bursts has visibly different frequency-drift rates on dynamical spectra of radio observations. The same is related to type IV bursts, radiation of which involves acceleration of electrons trapped in magnetic arches. The magnetic arches can be stretched and compressed by CMEs [2]. Of the sporadic radio emission from the Sun, the type III bursts are likely most indicative of eruptions of energetic particles. They provide important diagnostics of the ambient medium through which the solar disturbances propagate and can be used as natural plasma probes traversing the corona. Note, our understanding of the bursts and their relations to CMEs are far from perfect.

Although type III bursts are observed from 500 MHz to tens kilohertz, they do not always show a frequency drift from the highest frequencies to very low ones. In particular, the low-frequency cut-off of solar bursts in the ground-based observations is imposed by the ionosphere. On the other hand, as it is well known (see, for example, [3]), often the bursts observed at metric wavelengths are not observed at decametric range of wavelengths, and on the contrary many bursts are not observed at hectometric and kilometric wavelengths and are clearly detected in ground-based observations at decametric wavelengths. The reasons for these cut-offs have not fully understood yet. In this report we consider the solar bursts with high-frequency cutoff at decametric wavelengths, and a possible source of such burst radio emission is discussed as applied to the interpretation of their cut-off features.

OBSERVATIONS

During this observation the UTR-2 radio telescope was operated in the mode includes four sections of the north-south array of the antenna. The total effective area of these four sections is 50 000 m^2 with the beam pattern size of 1°×15° at 25 MHz. On 17-19 August 2012 we observed some tens of solar bursts with high-frequency cut-off. Their frequency cut-off varies from event to event in the range 14-30 MHz, and the frequency drift rate was from 0.3 MHz/s up to some ones MHz/s. Sometimes the bursts show a fine structure similar to bright filaments with small frequency drift rate. Therefore, they were even named "caterpillar" in [4]. The bursts with high-frequency cut-off are characterized by a relatively low degree of polarization about 10 % [5] that points out to their occurrence at the second harmonic relative to the local plasma frequency. Figure 1 shows the dynamic radio spectrum of one example of them at 8:16 UT on 18 August 2012. The data were recorded by the digital DSP spectrometer operating in the frequency range of 8-33 MHz with a frequency-time resolution in 4 kHz and

100 ms, respectively. The given burst has the frequency drift rate about -0.46 MHz/s, and the noticeable frequency of cut-off is 16. ± 1 MHz, although some weak details of radio emission occur at higher frequencies. Its flux achieved 240 s.f.u. (1 s.f.u. = 10^{-22} W/(Hz m^2)). In this event we can distinguish two components. One of them has the duration about 20 s at 10 MHz and 8 s at 16 MHz, and the second component lasts 14 s.

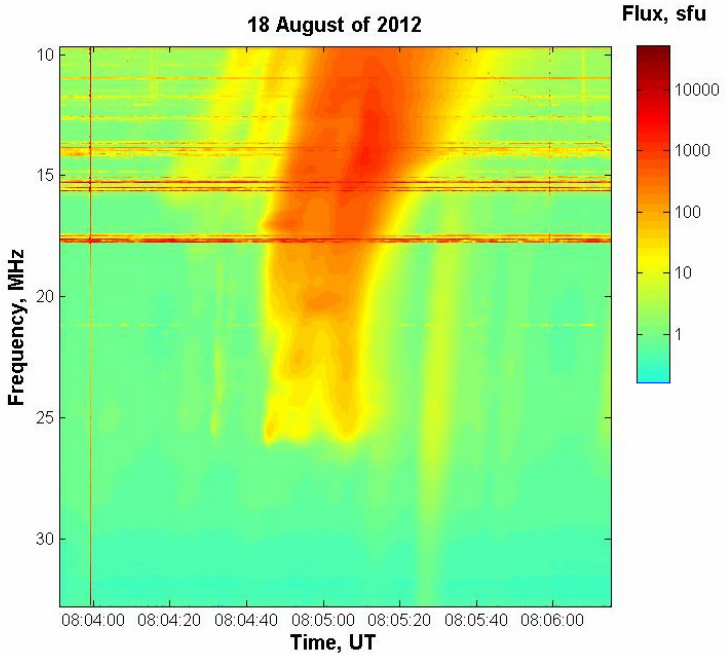

Figure 1: An illustrative example of the bursts with high-frequency cut-off on 18 August 2012. The horizontal bright lines on the dynamic spectrum indicate intensive disturbances due to broadcast radio stations.

On 17-19 August 2012 many C-class and M-class X-ray flares, following each other, were observed (see Figure 2 as an example) by STEREO, GOES and SOHO spacecrafts. The solar activity is also accompanied with CMEs emerging near the solar limb, if the events are viewed toward the Earth. They were connected with NOAA active region 11548 invisible from the Earth.

PROBLEM

The simplest interpretation of the cutoff leads to the conclusion that the location of their radiating sources is behind the Sun relative to an observer on Earth, and the bursts are emitted at the second (H) harmonic of the local plasma frequency [4]. Then the high-frequency radiation part is hidden (occulted) by the solar corona. However, this explanation needs to be clarified. In this connection also it should be accounted for the refraction of radio emission in coronal plasma. Because of this effect the ray tracing from the burst sources, located behind the solar limb, may be directed away from the Earth.

Really, from the refractive index variation with height in the solar corona, the path of a radio emission ray is calculated with help of the Snell's law [6, 7]. Without loss of generality we assume the spherical symmetry that simplifies the ray tracing calculations. The refractive index is written as $n^2 = 1 - f_{pe}^2 / f^2$, where $f_{pe} = 8.98\sqrt{N_e}$ is the electron plasma frequency in kHz, and N_e (cm^{-3}) describes the electron density of the solar corona in dependence of the distance ρ from the center of the Sun. The point (ρ, θ) of the ray tracing obeys the equation

$$\theta = a\int_{\rho}^{\infty} \frac{d\rho}{\rho\sqrt{n^2\rho^2 - a^2}},$$

where a is the distance of the asymptote of the ray for large ρ with $n=1$. Here θ is the angle between the line through the center of the Sun, parallel to the asymptote, and the direction on the ray position [6]. As the radius of the Sun is 109 times the radius of the Earth, the value a becomes very small (close to zero) in our study. It is not difficult to show that in this case the angle θ is proportional to a for any model of the solar electron density. This means that the value $\theta \geq \pi/2$ requires a special case of the electron density variation with height in the solar corona, namely the refractive index should be close to one. Therefore, the scheme of propagation of post-limb radio emission, if it is watched on the Earth, should be developed in a new way. In this problem we notice the important contribution of CMEs that took place near the solar limb. Their occurrence strongly is correlated with the emergence of solar bursts with high-frequency cut-off.

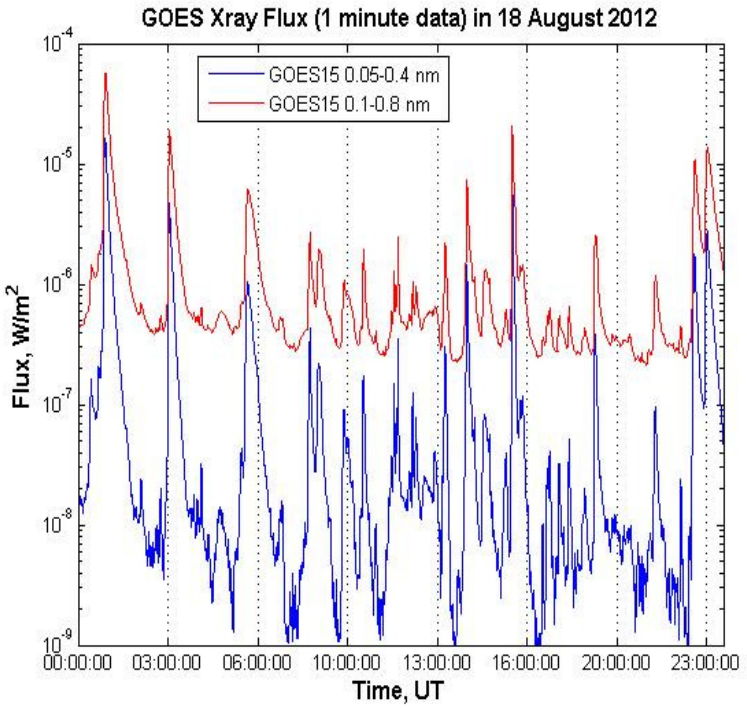

Figure 2: A time series of solar X-ray emission observed by the GOES-15 on 18 August 2012.

RESULTS

As a CME emerges, it typically contains a lower-density cavity behind its crest (dark bands at LASCO frames), and it often has a bright prominence core embedded within it [8]. The interesting feature of CMEs indicates that they may form tunnel-like cavities with low density. Under appropriate conditions this permit burst sources, moving behind the solar limb (relative to an observer on the Earth), to emit radio signals towards the Earth through or due to such cavities (Fig. 3). Probably, the radiation is observed in ground-based observations as solar bursts with high-frequency cut-off.

Based on the study, we guess that the bursts with high-frequency cut-off are nothing else, but type III radio bursts. However, since their source is located behind the solar limb toward the Earth, the effects of radio wave propagation in tunnel-like cavities of the solar corona can distort the observed frequency-drift rate of the bursts. This explains why some of them have the frequency drift rate as one in type III radio bursts, and others are not. Moreover, the duration of the behind-limb bursts may be somewhat more than one typical for type III bursts at decametric wavelengths because of the confluence of several nearby bursts with delay.

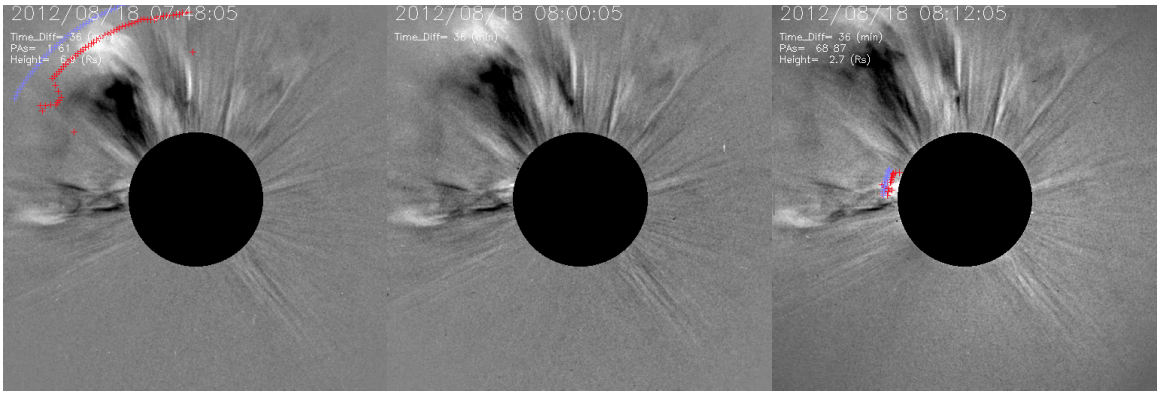

Figure 3: Image of the solar corona, taken by the LASCO coronagraph (C2) on the SOHO observatory. Image courtesy of the SOHO team.

ACKNOWLEDGEMENTS

We thank the GOES and SOHO teams for developing and operating the instruments and we are grateful for their open data policy. This research was partially supported by Research Grant "Synchronized simultaneous study of radio emission of solar system objects by low-frequency ground- and space-based astronomy" from the National Academy of Sciences of Ukraine.

REFERENCES

[1] N. Gopalswamy, "Coronal Mass Ejections and Solar Radio Emission", in Planetary Radio Emissions VII, H.O. Rucker, W. S. Kurth, P. Louarn, and G. Fischer, Eds. Austrian Academy of Sciences Press, Vienna, pp. 325-342, 2010.

[2] A.A. Konovalenko, A.A. Stanislavsky, et al., "Absorption in Burst Emission", Solar Phys., vol. 245, pp. 345–354, 2007.

[3] H. Alvarez, F. Haddock, and R.P. Lin, "Evidence for Electron Excitation of Type III Radio Burst Emission", Solar Phys., vol. 26, pp. 468-473, 1972.

[4] V.N. Melnik, A.I. Brazhenko, et al., "Unusual Solar Radio Burst Observed at Decameter Wavelengths", Solar Phys., vol. 289, pp. 263-278, 2014.

[5] A.I. Brazhenko, private communication, 2014.

[6] R.N. Bracewell, and G.W. Preston, "Radio Reflection and Refraction Phenomena in the High Solar Corona", Astrophys. J., vol. 123, pp. 14-29, 1956.

[7] G. Thejappa, and R.J. MacDowall, "Localization of a type III burst observed by the STEREO spacecraft", Astrophys. J., vol. 720, pp. 1395-1404, 2010.

[8] S.E. Gibson, T.A. Kucera, et al., "Three-dimensional Morphology of a Coronal Prominence Cavity", Astrophys. J., vol. 724, pp. 1133-1146, 2010.

Advances in solar bursts observations by the low-frequency radio telescopes of a new age

I.N. Bubnov, A.A. Stanislavsky, A.A. Konovalenko, S. Yerin,
A.A. Gridin, A.A. Koval
Institute of radio astronomy national academy of sciences of Ukraine
E-mail: boobnov@mail.ru

ABSTRACT

Observations of solar radio emission and the impact of solar activity on the space weather is one of the hot topics in astrophysics today. In particular, a great variety of the bursts is observed at frequencies below 100 MHz. This paper is devoted to a new sub-array of Giant Ukrainian Radio Telescope (GURT) and recent results obtained with this instrument as applied to the study of sporadic solar radio emission within 10-70 MHz range. Wideband observations at decameter-meter wavelengths considerably extend the possibility in registrations of rare solar events. The examples of such phenomena recorded in 2012 and 2014 are given. The study of ionosphere scintillations of cosmic radio sources well adds the analysis of solar events.

INTRODUCTION

Observations of solar radio emission and the influence of solar activity on interplanetary medium, magnetosphere, ionosphere and atmosphere of the Earth is one of the most important task today. Such observations should be carried out in a wide frequency range and with high time-frequency resolution to detect a fine structure of sporadic radio bursts. A great variety of the bursts is observed at frequencies below 100 MHz. This is one of the main reasons to devote so much observational time for the study of solar radio emission in scientific programs at modern low-frequency instruments such as LOFAR, LWA and so on [1].

OBSERVATIONS

A short description of the sub-array of new low frequency Giant Ukrainian Radio Telescope (called briefly GURT) and recent results of radio astronomy observations with help of this instrument within 10-70 MHz range are presented [2,3]. Examples of solar III and III-B type bursts are shown. A very rare phenomenon, the solar low-frequency U-burst, which is generated by electrons moving along closed magnetic field lines at solar corona, has been registered [4]. Wideband observations in decameter and meter wavelengths ranges considerably raise the probability of burst registrations in harmonic pairs. Such pairs are generated at first and second harmonics of electron plasma frequency. Examples of the phenomena registered in 2012 and 2014 are given. In addition the records of ionosphere scintillations of cosmic radio sources which can be used for studies of ionosphere conditions in the place of radio astronomy observations are presented.

CONCLUSION

The presented results show that the built GURT sub-array can be used for intensive studies of sporadic solar radio emission as well as ionosphere scintillations. Further extending of GURT radio telescope effective area with building new additional sub-arrays will allow increasing the spatial resolution for solar observations and using methods of both ionosphere and interplanetary scintillations for measuring the parameters of ionosphere and interplanetary media (study of solar wind).

REFERENCES

[1] S. M. White, N. E. Kassim, and W. C. Erickson, Solar radioastronomy with the LOFAR (LOw Frequency ARray) radio telescope, in Innovative Telescopes and Instrumentation for Solar Astrophysics, vol. 4853 of Proceedings of SPIE, pp. 111–120, Waikoloa, Hawaii, USA, August 2002.

[2] A.A. Konovalenko, I.S. Falkovich, N.N. Kalinichenko, A.A. Gridin, I.N. Bubnov, A. Lecacheux, C. Rosolen, H.O. Rucker, Thirty-element active antenna array as a prototype of a huge low-frequency radio telescope, Experimental Astronomy, vol. 16, no. 3, pp. 149–164, 2003.

[3] A. A. Stanislavsky, I. N. Bubnov, A. A. Konovalenko, A. A. Gridin, V. V. Shevchenko, L. A. Stanislavsky, D. V. Mukha, and A. A. Koval, First Radio Astronomy Examination of the Low-Frequency Broadband Active Antenna Subarray, Advances in Astronomy, Vol. 2014 (2014), Article ID 517058, 5 p., http://dx.doi.org/10.1155/2014/517058.

[4]. V. Dorovskyy, V. Melnik, A. Konovalenko, I. Bubnov, A. Gridin, N. Shevchuk, H. Rucker, S. Poedts, and M. Panchenko, Decameter U-burst Harmonic Pair from a High Loop, Solar Phys., Vol. 290 (1), pp. 181-192, 2015.

Analysis of the Nonlinear Behavior of the Accretion Flows

Krasimira Yankova[1]

[1] Space Research and Technology Institute – Bulgarian Academy of Sciences
E-mail: *f7@space.bas.bg*

Abstract

In this paper a research of the accretion flow structures in disks on Cyg X-1 and SgrA* have been done. We analyze the behaviour on the advective hypothesis. We discuss influence of the self-induction advection over components on the systems disk - corona in these real objects.

Introduction

We have developed a new model of the accretion disc's magneto-hydrodynamics, based on some specific advective hypothesis, presented in Yankova (2013, 2015). We constructed geometrically thin, optically thick, one-temperature Keplerian disc in a normal magnetic field, around a black hole.

The results of the model, given in detail in Iankova (2007a, b), Iankova (2009), Yankova (2012a, b, c), we presented global model for radial and vertical structures of disk; model for local structure and adaptation of the model for the conditions of emerging corona.

Results and analyze

We applied the model in real sources, and we will analyze the results for the nature of the flow in them.

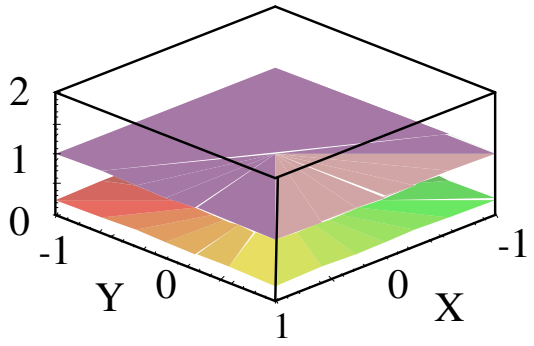

Fig.1a: Distribution $f_3(X,Y)$ of the dimensionless function of the sound velocity $f_3(x,\varphi)$ in the plane disc (X,Y) at $t=1P\sim\Omega_0^{-1}$.

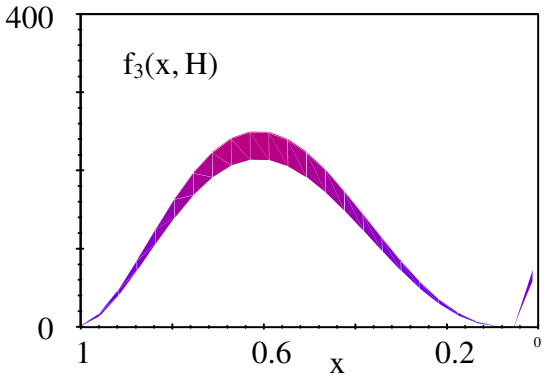

Fig.1b:Distribution $f_3(X,H)$ of the dimensionless function of the sound velocity $f_3(x,Z)$ on the border between the corona and disc.

The results for the sound velocity (Figure 1a) indicate that the function forming two well-distinguishable independent main branches. This means that a period after spreading of the disc it starts forming compacting zones - rings with a higher density relative to the environment. Local model of these formations determine clearly their advective character and distinguish them uniquely from the spirals on the disc.

In the binary, the branch of advective rings was layered additional (Figure 2a), which means secondary packing of the radiation in the flow from the fluidic optical fibers formed in the disc. In the disk of galactic core, ring-like areas remain unilamellar (fig.2b) and as shows the continuity of the surfaces of the two branches of the function, advective rings and both cases are mobile in accordance with their physical selves.

$$\frac{\partial(\rho \boldsymbol{v}_i)}{\partial t}+\frac{\partial}{\partial x_j}(\rho \boldsymbol{v}_i \boldsymbol{v}_j)=\rho\left(\frac{\partial \boldsymbol{v}_i}{\partial t}+\boldsymbol{v}_j\frac{\partial \boldsymbol{v}_i}{\partial x_j}\right)=\rho\frac{\boldsymbol{D}\boldsymbol{v}_i}{\boldsymbol{D}t} \qquad (1)$$

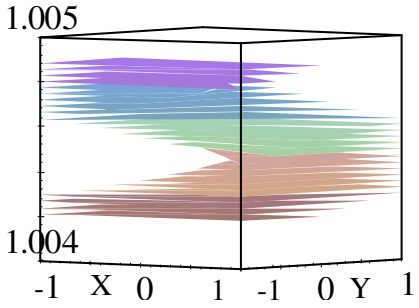

Fig.2a: Distribution $f_3(X,Y)$ of the dimensionless function of the sound velocity $f_3(x,\varphi)$ in the plane disc (X,Y) at t=1P~Ω_0^{-1}, for Cyg X-1.

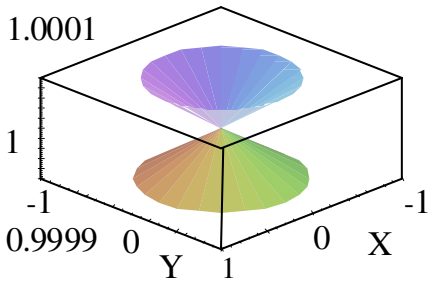

Fig.2b: Distribution $f_3(X,Y)$ of the dimensionless function of the sound velocity $f_3(x,\varphi)$ in the plane disc (X,Y) at t=1P~Ω_0^{-1}, for SgrA*.

By the development of the components of the magnetic field provides information about the microstructures present in the stream, and their behaviour.

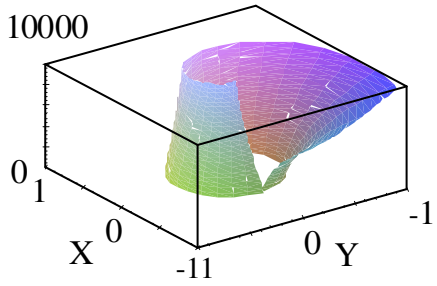

Fig.3a: Distribution $f_5(X,Y)$ of the dimensionless function of the radial field $f_5(x,\varphi)$ in the plane disc (X,Y) at t=1P~Ω_0^{-1}, for Cyg X-1.

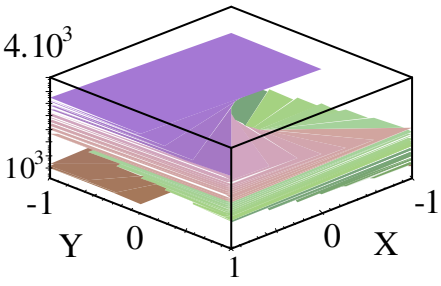

Fig.3b: Distribution $f_5(X,Y)$ of the dimensionless function of the radial field $f_5(x,\varphi)$ in the plane disc (X,Y) at t=1P~Ω_0^{-1}, for SgrA*.

In Cyg X-1 amplified asymmetry is observed in $\mathbf{B}_r$ (fig.3a). The function does not show clustering around discrete values in increase, what we see in Sgr A * (fig.3b). The projection of $f_6(x, \varphi)$ (fig.4b) indicates that the disc has a plurality of different sized loops - both positive and negative relative to the direction of flow. All this means continuous cascade that maintains the negative gradient of entropy and with it the self-induction in the advection.

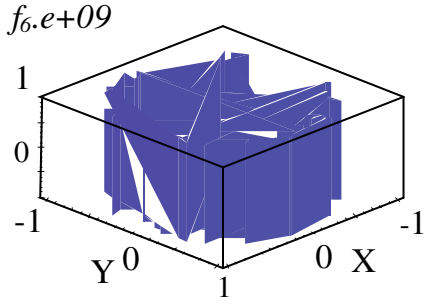

(a)

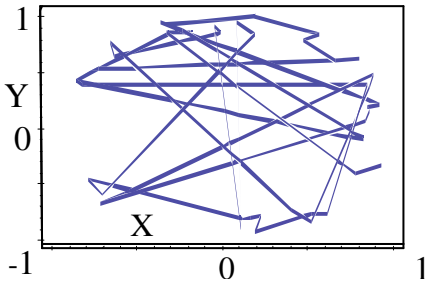

(b)

(c)

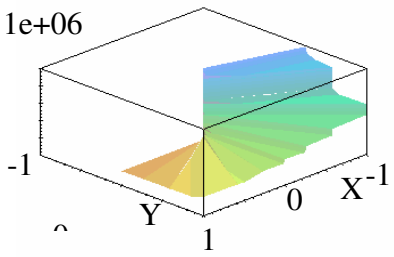

Fig.4: Distribution $f_6(X,Y)$ of the dimensionless function of the azimuthal field $f_6(x,\phi)$ in the plane disc (X,Y) at $t=1P\sim\Omega_0^{-1}$, for Cyg X-1 (4a, b). And SgrA*(4c).

The behavior of the function $\mathbf{B}_r$ at Sgr A * (fig.3b) shows the existence of different groups MPH, with the exchange of energy between the low and high harmonics in the spectrum (see also the leaps increasing on $f_6(x, \varphi)$ (fig.4c)). This is fragmented and consolidated of loops, accompanied with absorbing energy from the environment during the above-mentioned exchange. Growing microstructures compensate the effects of negative entropy gradient (fig.6b), as absorb energetic surplus. This reserve ensures the reemergence of the ML from plasma in another way, and with this explains simplified advective rings on this disc.

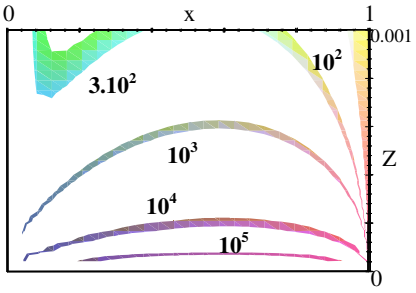

Fig.5a: Profile in the plane (x, Z) of the sound velocity for the point of inflow $\phi_0 = 0$, at the time $t = 1P \sim\Omega_0^{-1}$, in $f_3(x, Z)=10^2; 3.10^2; 10^3; 10^4; 10^5$, for Cyg X-1.

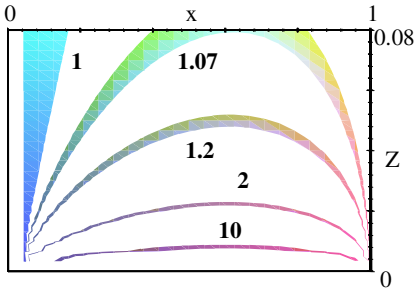

Fig.5b: Profile in the plane (x, Z) of the sound velocity for the point of inflow $\phi_0 = 0$, at the time $t = 1P \sim\Omega_0^{-1}$, in $f_3(x,Z) =1; 1.07; 1.2; 2; 10$, for SgrA*.

Vertical distribution of sound velocity is especially sensitive to the exchange and distribution of energy in the disk, which is controlled by the overall interaction between parameters and the impact of nonlinear effects on them. Arched contours in the vertical structure of the disk show that in the inner regions of a re-stabilization of the stream, which is confirmed by the recovery of the positive gradient of entropy (fig.5-6). This stabilization was mainly due to the emerging corona.

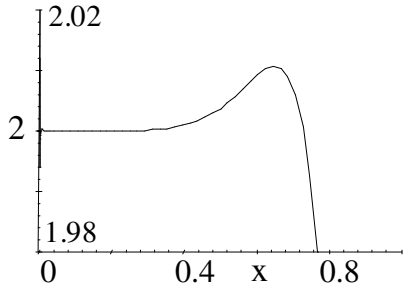

Fig.6a: Development of the gradient of entropy in Cyg X-1.

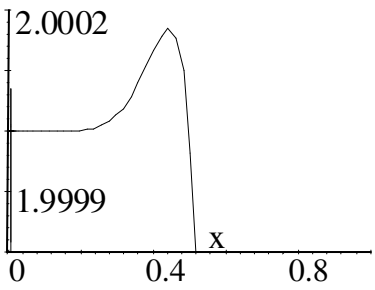

Fig.6b: Development of the gradient of entropy in SgrA*

Conclution

In this paper, we use the results of the theoretical model of the disk, to description of the processes in the disk and on boundary with the corona at two real objects. Advective rings which provide the warming of the pad, determine the type of the border with the corona.

At Cyg X-1 rings of this type contribute to form a sharp boundary between the disc and the corona and both components of the system can be considered individually.

Cannibalism of instabilities in the disk of SgrA* and incomplete re-stabilization of the stream (as opposed to micro-quasar) talked about fuzzy border. Components is well be considered complex there, but still can be considered individually depending on the degree of fuzziness of the border.

These results are another step in the direction of for creating full model of the system disk-corona. Also, tool for determining the degree to which the main component influenced the development of coronary component.

References

Iankova Kr. D.: 2007a, BSSPP Proc. Ser. 1, pp 143-146.

Iankova Kr. D.: 2007b, 5th Bulgarian-Serbian Conference (V BSCASS): "Astronomy and Space Science", Heron Press Ltd.Science series, pp 326-29.

Iankova Kr. D.: 2009, Proc. VI Serbian-Bulgarian Astronomical Conference, Publ. Astr. Soc. "Rudjer Boљkovi ", No. 9, 327-333.

Yankova Kr. D.: 2012a, SSTRI-BAN, SENS 2011 proceedings, ISSN 1313-3888, 73-78.

Yankova Kr.D.: 2012b, Publications of the Astronomical Society "Rudjer Boskovic", vol. 11, pp.375-383. Hhttp://adsabs.harvard.edu/abs/2012PASRB..11..375YH

Yankova Kr.D.: 2012c, JUBILEE INTERNATIONAL CONGRESS: SCIENCE, EDUCATION, TECHNOLOGIES "40 YEARS BULGARIA – SPACE COUNTRY ", proceedings (ISBN 978-954-577-636-6), Tom1, 152-158.

Yankova Kr.D.: 2013, Proceedings of the VIII Serbian-Bulgarian Astronomical Conference (VIII SBAC), Publ. Astron. Soc. “Rudjer Bošković” vol. 12, 375-381. Hhttp://wfpdb.org/ftp/8_SBAC_D1/pdfs/34.pdf

Yankova Kr.: 2015, Bulgarian Astronomical Journal, Vol. 22, p. 83. http://adsabs.harvard.edu/abs/2015BlgAJ..22...83Y

Delayed response of global TEC to ionization variations seen from combined SolACES-SDO/EVE solar EUV spectra

Jacobi Ch [1], *Unglaub C* [1], *Schmidtke, G* [2], *Pfeifer M* [2], *Schäfer R* [2], *Brunner R* [2], *Woods T* [3], *Jakowski N* [4]

[1]Institute for Meteorology, Universität Leipzig , [2]Fraunhofer IPM, Freiburg, [3]LASP, University of Colorado, Boulder, CO, [4]German Aerospace Center, Neustrelitz
E-mail: jacobi@uni-leipzig.de

INTRODUCTION

The solar extreme ultraviolet (EUV) radiation varies on different time scales, including the 27-day Carrington rotation as one of the primary sources of variability at the intra-seasonal time scale. Consequences are strong changes of ionization of the Earth´s upper atmosphere, and corresponding variability of the electron density and also the Total Electron Content (TEC). TEC variability is a coarse estimate for ionization as well, so that indices describing EUV and ionization may be compared against ionospheric TEC. Such indices may be obtained from integrating observed EUV spectral solar flux, e.g. from the SDO/EVE experiment (Woods et al., 2012) in the relevant wavelength range. Unglaub et al. (2011) have introduced a proxy, termed EUV-TEC, which is based on the vertical and globally integrated primary ionization rates calculated from observed EUV spectra.

However, correlation of parameters describing ionospheric electron density and EUV proxies is not always strong at time scales of the solar rotation, and several studies report a delayed response of the ionospheric plasma density to solar activity changes (e.g. Jakowski et al., 1991; Lee et al., 2012). Therefore, this ionospheric delayed response is analyzed here, and taken into account in the EUV proxies.

EUV proxy and analysis of delay

We calculate a daily EUV proxy as the SDO/EVE Version 5 data integrated between 16.5 and 105.5 nm. Daily global mean TEC values have been calculated based on IGS TEC maps (Hernandez-Pajares et al., 2009) in order to evaluate this EUV proxy. The data were normalized by subtracting the mean and dividing by the standard deviation from January 20, 2011 through March 10, 2014 (approx. Carrington rotations 2106 - 2147). The mean values and standard deviations are 3.822±0.387 mWm^{-2} for SDO/EVE fluxes, and 24.41±6.05 TECU for global TEC. Figure 1 presents the normalized EUV flux and global TEC from 2011 through early 2014. The observations cover part of solar cycle 24, with generally increasing solar flux and consequently ionospheric TEC. The time series is too short to investigate the 11-year solar cycle. Generally there is good agreement of TEC and EUV at the interannual time scale. At the seasonal time scale there are some discrepancies owing to the semiannual TEC cycle which is not seen in EUV. At the 27-day time scale of the solar rotation there is considerable agreement between the time series when the amplitudes are large, although the amplitudes not always correspond to each other.

In order to analyze the correlation of TEC and EUV proxies at different time scales, we filtered the normalized data using a Lanczos bandpass filter with 100 weights. In Figure 2, part of the time series of SDO/EVE integrated fluxes and TEC are presented for time scales of 2-90 days and for 24-28 days. The variability is mainly determined by the 27-day solar rotation, and a time delay is visible between the EUV flux (black) and TEC (red). The squared correlation coefficient between normalized TEC and EUV at the time scales 2-90 days is $r^2 = 0.75$. Longer time scales than 90 days will not be considered here, because these are dominated by the annual cycle, which is different for TEC and solar radiation, and part of the 11-year cycle.

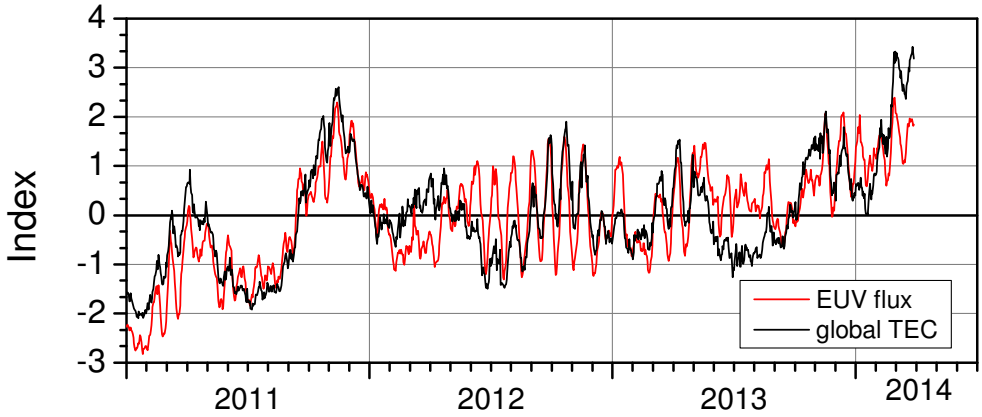

Figure 1: Normalized integrated EUV flux from SDO/EVE Version 5 spectra and global TEC.

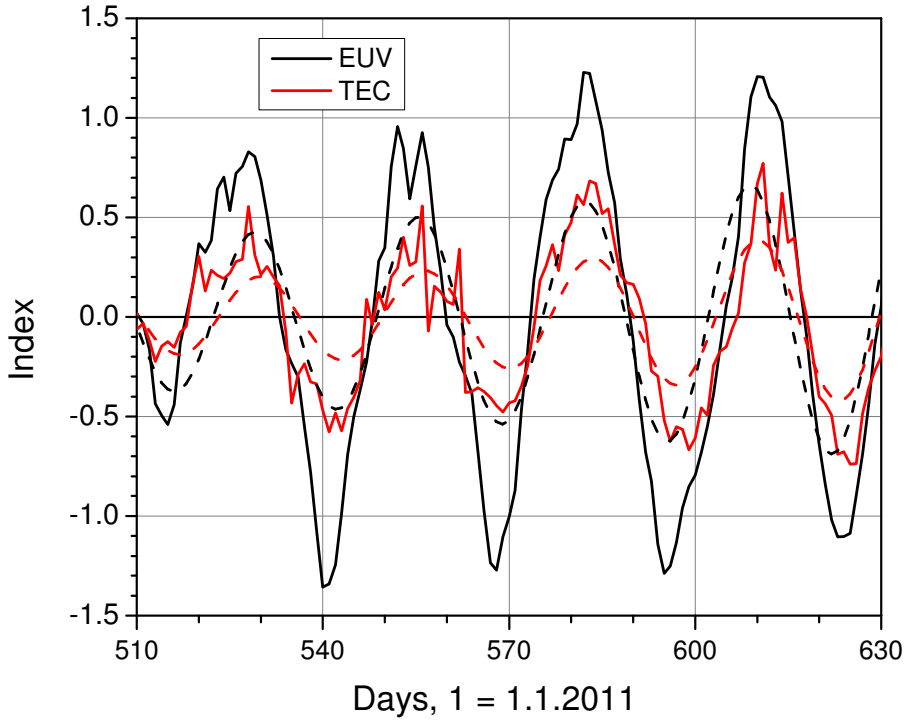

Figure 2: Time series of EUV integrated fluxes and global TEC in different the 2-90 days (solid) and 24-28 days (dashed) period bands.

To systematically investigate the delay at different time scales, we now filtered the time series in different period bands, and the cut-off periods of the Lanczos filter were chosen in such a way that each period band ranges over 4 days, while the centre of the period band was shifted from 4 to 88 days. For each pair of filtered time series, i.e. for each time scale, the cross-correlation function is shown in Figure 3. Positive values indicate that TEC variations lag EUV ones. Solid blue dots are added that show the time lag with maximum correlation which can, however, only be provided at an accuracy of one day. We also analyzed a EUV-TEC proxy after Unglaub et al. (2011), based on the combined SDO/EVE and SolACES (Schmidtke et al., 2014) spectra in this wavelength interval. EUV-TEC is calculated as the primary ionization using a NRLMSISE-00 (Picone et al., 2002) model atmosphere. The proxy is defined as the daily vertically and globally averaged ionization rates normalized by their time mean and standard deviation. The ionization rates were normalized by their mean and standard deviations being $1.180 \cdot 10^{19} \pm 1.23 \cdot 10^{18}$ ions/m^2. The lag of maximum correlation between this proxy and global TEC are also shown in Figure 3 as light blue dots.

Figure 2 shows that at short time scales of few days, the correlation is weak. At time scales of the solar rotation, the strongest correlation is found and global TEC lags EUV flux variations by about one day. The lag increases a bit for time scales around 2 months. For the EUV-TEC proxy, the lag at time scales of about 2 months is slightly longer. Differences to directly using SDO/EVE fluxes may be due to the fact that the EUV-TEC proxy uses the NRLMSIS-E atmosphere, which is calculated using the F10.7 solar index. At longer time scales than the solar rotation, the effect of seasonal variations of the background atmosphere will affect the proxy.

To improve the correlation between TEC and EUV flux, we shifted the TEC time series by one day. Taking into account that the time resolution of the datasets allows only a coarse approach, we did not consider small structures in the time lag at different time scales as they are visible in Figure 3. When using the shifted TEC time series, the squared correlation between normalized TEC and EUV increases to $r^2 = 0.81$.

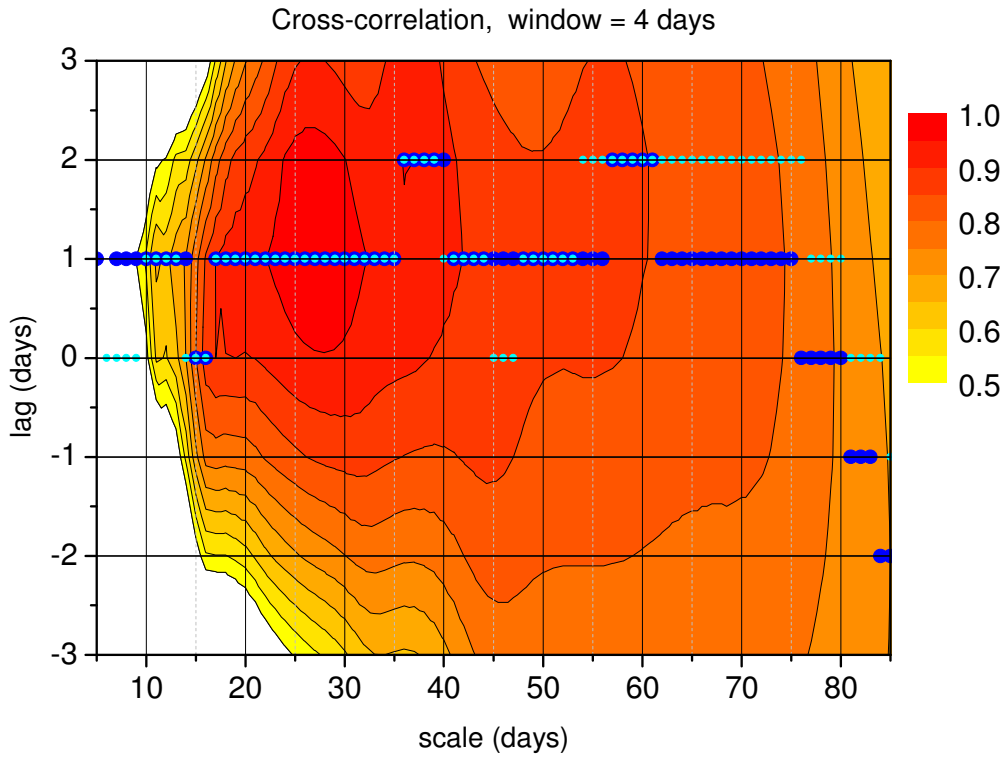

Figure 3: Cross-correlation coefficients between global TEC and SDO/EVE integrated fluxes. The scale is the centre of the 4-day period band of the respective filter. Positive values indicate that TEC variations lag EUV ones. Solid dark blue dots show the lag with maximum correlation at an accuracy of one day. Light blue dots are added that indicate maximum correlation between TEC and the EUV-TEC primary ionization proxy based on SDO/EVE and SolACES combined daily EUV spectra.

Conclusions and outlook

When taking into account the ionospheric delay at the solar rotation time scale, proxies to describe the influence of EUV on ionization rates can be improved. The results presented here are preliminary. We used daily EUV spectra and daily and globally averaged TEC, which gives only coarse values for the time lag. TEC maps are available at higher temporal resolution, and EUV fluxes at least for some spectral bands are also available. This will provide the possibility to study ionospheric delay at higher temporal and spatial resolution.

Acknowledgements: TEC data has been provided by NASA through ftp access on ftp://cddis.gsfc.nasa.gov/gps/products/ionex/.

REFERENCES

Hernandez-Pajares, M., Juan, J.M., Sanz, J., Orus, R., Garcia-Rigo, A., Feltens, J., Komjathy, A., Schaer, S.C., Krankowski, A., 2009: The IGS VTEC maps: a reliable source of ionospheric information since 1998, J. Geod. 83, 263–275.

Jakowski., N., Fichtelmann, B., Jungstand, A., 1991: Solar activity control of ionospheric and thermospheric processes. J. Atmos. Terr. Phys., 53, 1125-1130.

Lee, C.-K., Han, S.-C., Bilitza, D., Seo, K.-W., 2012. Global characteristics of the correlation and time lag between solar and ionospheric parameters in the 27-day period. J. Atmos. Sol.-Terr. Phys, 77, 219–224, doi:10.1016/j.jastp.2012.01.010.

Picone, J.M., Hedin, A.E., Drob, D.P., 2002: NRLMSISE-00 empirical model of the atmosphere: statistical comparisons and scientific issues, J. Geophys. Res., 107, 1468, doi:10.1029/2002JA009430.

Schmidtke, G., Nikutowski, B., Jacobi, Ch., Brunner, R., Erhardt, Ch., Knecht, S., Scherle, J., Schlagenhauf, J., 2014: Solar EUV irradiance measurements by the Auto-Calibrating EUV Spectrometers (SolACES) aboard the International Space Station (ISS), Solar Phys., 289, 1863-1883, doi: 10.1007/s11207-013-0430-5.

Unglaub, C., Jacobi, Ch., Schmidtke, G., Nikutowski, B., Brunner, R., 2011: EUV-TEC proxy to describe ionospheric variability using satellite-borne solar EUV measurements: first results, Adv. Space Res., 47, 1578-1584, doi:10.1016/j.asr.2010.12.014.

Woods, T.N., Eparvier, F.G., Hock, R.; Jones, A.R., Woodraska, D., Judge, D., Didkovsky, L., Lean, J., Mariska, J., Warren, H., McMullin, D., Chamberlin, P., Berthiaume, G., Bailey, S., Fuller-Rowell, T., Sojka, J., Tobiska, W.K., Viereck, R., 2010: Extreme Ultraviolet Variability Experiment (EVE) on the Solar Dynamics Observatory (SDO): Overview of Science Objectives, Instrument Design, Data Products, and Model Developments, Solar Physics, 275, 115-143, doi: 10.1007/s11207-009-9487-6.

GEOMAGNETIC Pc1 PULSATION BEHAVIOR DEPENDING ON SOLAR ACTIVITY

Feygin F.Z., Malysheva L.M., Kleimenova N.G., Khabazin Yu.G.

Schmidt Institute of the Physics of the Earth RAS, Moscow, Russia
E-mail: kleimen@ifz.ru

Abstract

The latitude feature of Pc1 geomagnetic pulsations was studied on the base of the Scandinavian magnetometer chain near the maximum and minimum of the 24-th solar activity cycle. In the minimum (2008) there were about 30 magnetic storms, but in 2009 - only 5. The number of the hours with Pc1 was ~100 in 2008 and only ~20 in 2009. During the solar minimum, the shape of the Pc1 dynamic spectra was, generally, simple and the wave duration < 3-5 hours. However, during the declining (2006) and increasing (2010) solar activity stage, the spectral structure of Pc1 became more complicated and the wave duration increased up to 10-12 hours. We compared the total, right-hand and left-hand polarized Pc1 pulsations at two latitude spaced stations: SOD (Φ=63.8^0, L~5.3) and NUR (Φ=56.6^0, L~3.5). It was found that that in 2003 (near solar maximum), the Pc1 pulsations were stronger at NUR with left-hand polarization. It means that the station was located in vicinity of the wave exit point from the ionosphere. However, in the solar minimum, the Pc1 events were stronger at SOD and demonstrated the left-hand polarization too. Our finding supports the idea that the area of Pc1 wave generation could be related to the vicinity of the plasmapause.

Introduction

The Pc1 geomagnetic pulsations are the repeated wave packets of Alfven waves in the frequency range 0.2-5.0 Hz travelling between the conjugated hemispheres. Their theory of generation and the morphological properties are widely discussed in the literature last time in several revues [e.g. Kangas et al., 1998; Demekhov, 2007]. It is no doubt that Pc1 pulsations ("pearls") are generated via the cyclotron instability of radiation belt protons with anisotropic velocity distribution [e.g. Feygin and Yakimenko, 1971 and many others].

Here we present the analyzing results of the data obtained from the ground-based induction magnetometer network at Scandinavia), stored at (http://sgo.fi/Data/Pulsation/pulArchive.php). Figure 1 demonstrated the solar activity during the discussed period.

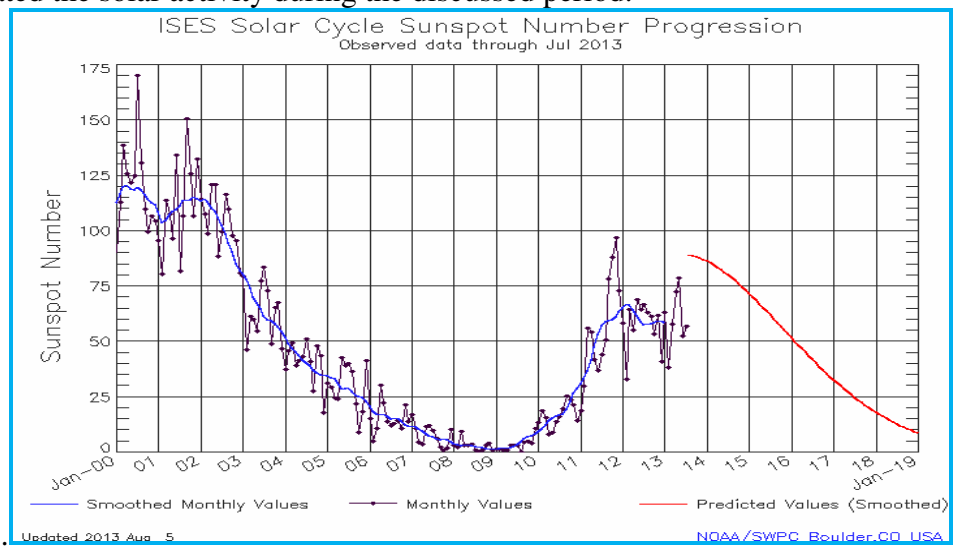

Fig.1. Solar activity (measured the Sunspot number) in 2001-2013 (blue line) and its prediction (red line).

Results of analysis

It is known, that the Pc1 occurrence maximum is observed in the declining phase of the solar activity. Really, in the declining phase of the 23-th cycle of the solar activity (2006), the number of the hours with long-lasting (more 2 hours) Pc1 series was ~270. In the minimum between 23-th and 24-th cycle, the lowest value of the Wolf number (Wp) ~ 3 was observed in 2008 and 2009. However, in 2008 there were two sequences of recurrent magnetic storms with 13-14 storms in each, but in 2009 there were only 5 small magnetic storms. Correspondingly, the number of the hours with long-lasting Pc1 series was ~100 in 2008 and it was~20 in 2009. It supports the relationship of long-lasting Pc1 generation with magnetic storms development.

The spectral structure of the Pc1 pulsations was different in quiet and disturbed magnetic conditions. An example of such events is presented in Fig. 2.

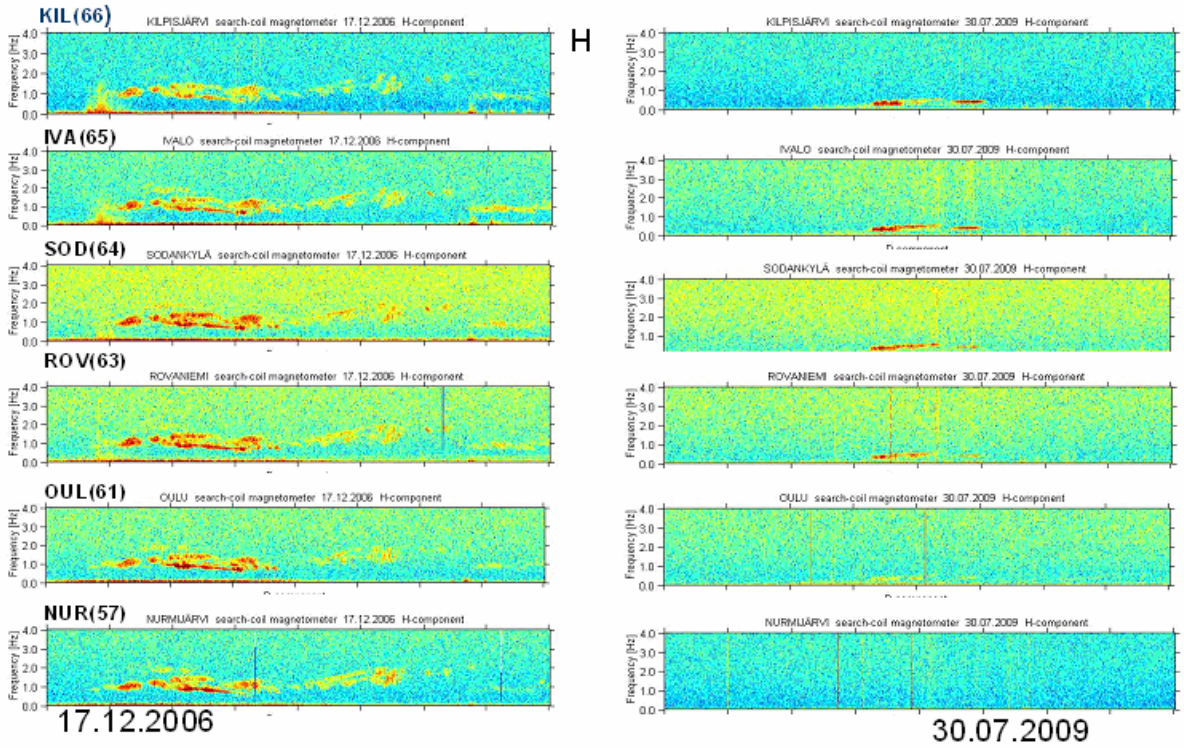

Fig. 2. The spectral structure of Pc1 pulsations under magnetically disturbed period (left panel) and under very quiet condition (right panel). The geomagnetic latitude of stations is shown behind the station cod.

As a rule, during the solar activity minimum, the shape of the frequency-temporal Pc1 spectra looked like a very monochromatic emission of not more 3-5 hours duration with a narrow of the width of the dynamic spectra. During the declining (2006) and increasing (2010) phases of the solar activity, the spectral structure of Pc1 pulsations became more complicated and the duration of the Pc1 series increased up to 10-12 hours. Sometimes it consisted of several varying frequency bands as it was demonstrated at the left panel of Fig. 2.

During the solar minimum (2008, 2009), the Pc1 pulsations are typically observed in the beginning of geomagnetic activity increasing after magnetically quiet (Kp ~ 0-1) periods, and the left-hand polarized pulsations were stronger in SOD (L~5.3) than in NUR (L~3.6), as it is shown in Fig.3. In such condition, the estimated plasmapause could be located according the model www.spaceweather.eu at L~5.0-5.5, thus, in vicinity of SOD station.

During the solar maximum (2003) Pc1 pulsations were observed generally in the recovery phase of magnetic storms and Pc1 waves were stronger in lower latitudes, e.g. in NUR (L~3.6) than in SOD (L~5.3). The examples are presented in Fig. 4. The wave

polarization in NUR was mainly left-handed (L). The estimated plasmapause location could be in the vicinity of NUR station.

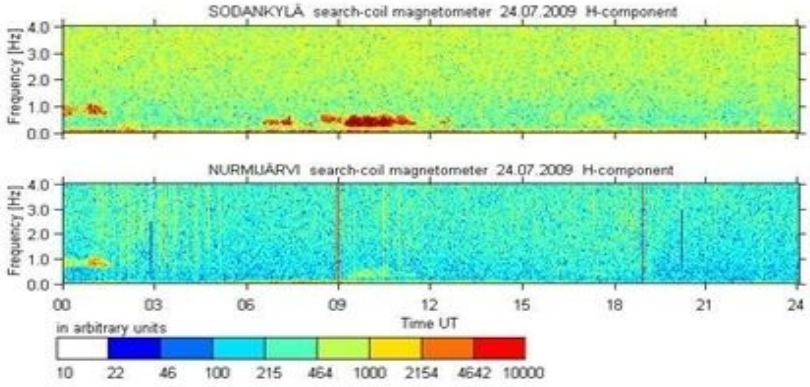

Fig. 3. Spectrograms of Pc1 pulsations in SOD and NUR stations

Discussion

The Pc1 pulsations propagate in the magnetosphere along geomagnetic field lines down to the ionosphere as left-hand polarized electromagnetic (Alfven) waves. Mapping through the ionosphere, these waves are seen on the ground near their footprint as the left polarized mode. Also the maximum of geomagnetic pulsation intensity is located in this region. Thus, the left-hand polarization of ground-based Pc1 indicates this station location in vicinity of Pc1 source footprint.

Right-hand polarized Pc1 waves on the ground could be related to the capture of Alfven waves into the ionospheric waveguide [e.g. Greifinger and Greifinger, 1968] and their convert into the fast magnetosonic ones with the wave polarization change from the left-handed to the right-handed. Another reason of right-hand polarized Pc1 wave appearance could be the availability of the heavy ions (mainly He^+ and O^+) in the magnetospheric plasma, leading to the emergence of so called the tunnel effect and the wave polarization reverse as it was observed, for example, on GEOS spacecraft [Perraut et al., 1984, Mikhailova, 2011]

Summary

The analysis of ground-based Scandinavian data showed:

1. The ground-based Pc1 pulsations (pearls) behavior is controlled by the solar activity level.
2. In the minimum of the solar activity (2008-2009), the shape of the Pc1 dynamic spectra was simple. However, during the declining (2006) and increasing (2010) solar activity stage, the spectral structure of Pc1 became more complicated and the wave duration increases.
3. During the solar minimum, the Pc1 events were stronger at higher latitudes, e.g. at SOD (L~5.3) than at NUR (L~3.5) and the plasmapause was mapped in the vicinity of SOD. The opposite situation was observed during the solar maximum: the Pc1 pulsations were stronger in NUR (L~3.6) than in SOD (L~5.3) and the plasmapause was mapped in the vicinity of NUR.
4. The wave polarization study can give us some additional information about the possible plasmapause location and its temporal dynamics.

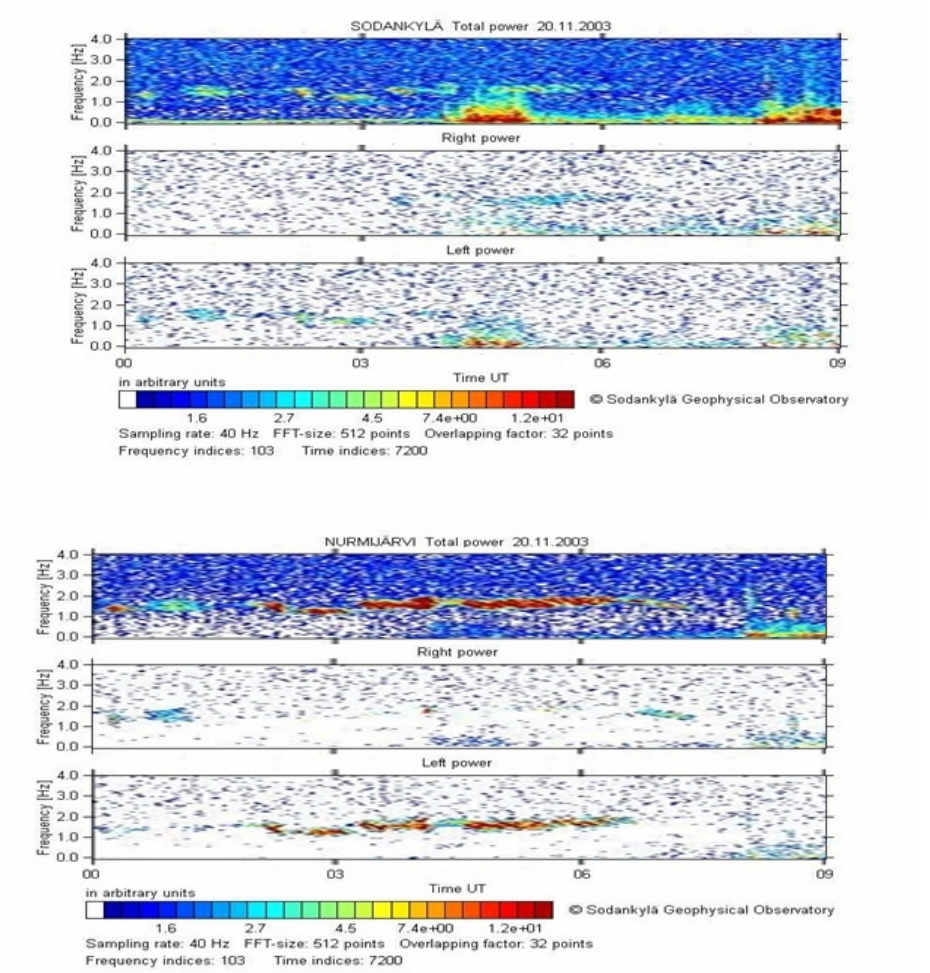

Fig. 4.Spectrograms of Pc1 pulsations in SOD (upper plots) and NUR (bottom plots); from top to bottom: total , right-hand and left-hand intensities.

Acknowledgements. The paper was supported by the Program No 9 of the Presidium of the Russian Academy of Sciences (RAS) and partly by the RFBR Grants № 15-05-07623 (F.F. and Yu.Kh.) and № 13-05-00233 (L.M. and N.K.)

References

Demekhov, A.G. Recent progress in understanding Pc1 pearl formation, *J. Atm. Solar-Terr. Phys.*, 69, 1609-1622, 2007.

Feygin, F.Z, and Yakimenko, V.L. Appearance and development of geomagnetic Pc1 type micropulsations ("pearls") due to cyclotron instability of proton belt, *Ann. Geophys*., 27, 49–55. 1971.

Greifinger, C. and Greifinger, P.S. Theory of hydromagnetic propagation in the ionospheric waveguide, *J. Geophys. Res*., 73, 7473-7490, 1968.

Mikhailova, O.S., On the possibility of localization of waves Pc 1 near ionosphere with the presence of heavy ions in the magnetosphere of the Earth, *Solar-terrestrial physics*, 19, 83-87, 2011.

Kangas, J., Guglielmi, A., and Pokhotelov, O., Morphology and physics of shortperiod magnetic pulsations, *Space Sci. Rev*, 83, 435–512, 1998.

Perraut S., Gendrin R., Roux A., and C. de Villedary. Ion cyclotron waves: direct comparison between ground-based measurements and observations in the source region,*J. Geophys. Res.,* 89 (A1), 195-202, 1984.

Geophysically Induced Currents, a space weather hazard. Case study – Europe under intense geomagnetic storms of the solar cycle 23

Crisan Demetrescu, Venera Dobrica, Cristiana Stefan, Razvan Greculeasa

Institute of Geodynamics, Romanian Academy
E-mail: crisan@geodin.ro

The interaction of the solar wind and heliospheric magnetic field with the magnetosphere and ionosphere results in variations of the geomagnetic field that induce hazardous electric currents in grounded technological systems (electric power and hydrocarbon transportation networks), the so-called GICs. In order to evaluate the hazard induced on the European continent, we present a study of the surface electric field induced by 16 intense (Dst < -150 nT) geomagnetic storms, based on the analysis of the geomagnetic records from the European network of observatories, study that tend to solve the geophysical part of the problem. The evolution during storm development and the sources of the disturbance field are explored in case of the largest geomagnetic storm in the cycle 23 (Dst = -422 nT, November 20-21, 2003), and the geographical distribution of the maximum induced surface geoelectric field over Europe by the 16 storms considered in the study is presented.

Data and method

1-minute values of the northward and eastward geomagnetic elements, recorded at up to 29 European observatories from the INTERMAGNET network during six days encompassing the 16 intense storms of the study (Table 1), were processed to get the time derivative that is driving the induced electric field.

Table 1

Year	Date	Dst (nT)	Year	Date	Dst (nT)
1998	May, 4	-205	2001	Apr, 11	-271
1998	Sep, 25	-207	2001	Nov, 5	-292
1999	Oct, 21	-237	2001	Nov, 24	-221
2000	Apr, 6	-287	2003	Oct, 29	-383
2000	Jul, 15	-301	2003	Nov, 20	-422
2000	Aug, 12	-235	2004	Nov, 7	-374
2000	Sep, 17	-201	2005	May, 15	-247
2001	March, 31	-387	2005	Aug, 24	-184

The induced electric field is assessed according to the method of Viljanen and Pirjola (1989), shortly reviewed in the next lines.

Generally, the horizontal electric field (Ex, Ey) produced by the variable magnetic field is linked to the magnetic field (Bx, By) through the impedance Z(ω) of the underground subject to the plane wave that approximate the propagation of the geomagnetic disturbance.

$$E_x(\omega) = \frac{Z(\omega)}{\mu_0} B_y(\omega), E_y(\omega) = \frac{Z(\omega)}{\mu_0} B_x(\omega)$$

For an Earth viewed as a halfspace with a conductivity σ, the surface electric field is described by

$$E_y(t) = -\frac{1}{\sqrt{\pi \mu_0 \sigma}} \int_{-\infty}^{t} \frac{g_x(u)}{\sqrt{t-u}} du ,$$

where g_x denotes the time derivative of the field B. The integral is converted to a sum that allows to calculate the 1-minute E values. A numerical code was written for the present study.

Two other methods to estimate the geographical distribution ofthe induced geoelectric field in a denser network of points is presently in use (Viljanen et al., 2014; Matandirotya et al., 2014).

Results

The largest storm of the sudy, namely – November 20-21, 2003, Dst = -422 nT – was produced by the interaction of the ICME, illustrated in Fig. 1 by the parameters of the solar wind recorded at the Lagrangean point 1 and available at http://omniweb.gsfc.nasa.gov/, with the magnetosphere. The evolution of the storm is illustrated in the same figure by means of the Dst geomagnetic index.

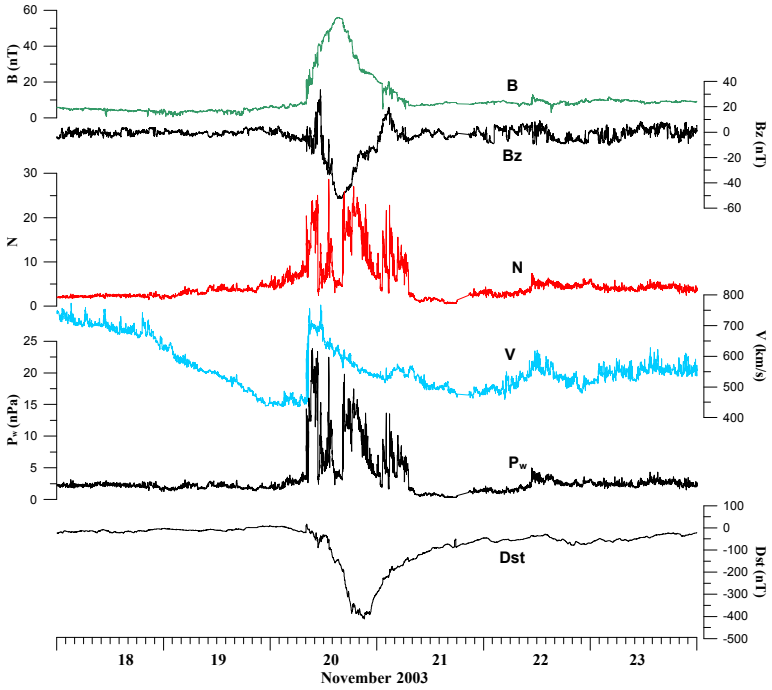

Fig. 1. Solar wind parameters and the Dst evolution for the November 2003 storm

To get an idea on the latitudinal differences that characterize the evolution of the geomagnetic field and of its time derivative, as well as of the induced surface geoelectric field during a geomagnetic storm, we show in Fig. 2 the results obtained for a longitudinal chain of observatories along the 105°E geomagnetic meridian. To show the extreme possible variations, the AL geomagnetic index, showing the disturbed field produced by the ionospheric electrojet at auroral latitude, and the Dst index, showing the disturbed field produced by the magnetospheric ring current at the geomagnetic equator, are plotted on top and, respectively, at the figure bottom.

Examining the figure several conclusions can be underlined, namely:

- the disturbance in Bx is 2-3 times larger at northern latitudes than at mid and southern latitudes;
- during the geomagnetic storm, effects of auroral electrojets superimpose at all latitudes on the disturbance created by the magetospheric ring current;
- the amplitude of the geoelectric field produced by magnetic variations is of the order of hundreths of mV/km in case of SUA (45°N), and of 1-2 mV/km in case of UPS (60°N);
- the more pronounced geoelectric component is directed East-West.

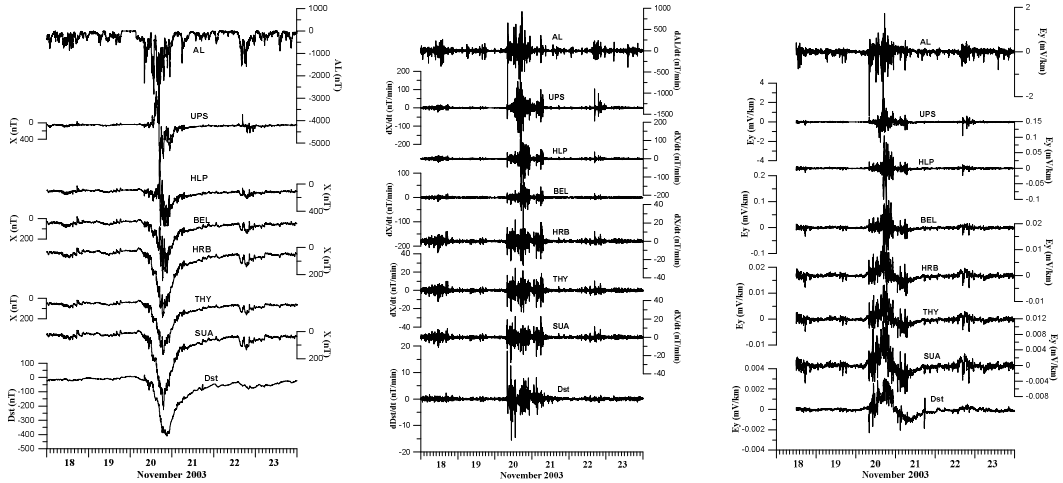

Fig. 2. The geomagnetic disturbance (Bx) (left), its time derivative (middle), and the resulting surface electric field (Ey) (right) for the November 2003 storm, at geomagnetic observatories along the 105°E geomagnetic meridian

As regards the sources of the variations observed, our study indicates both the magnetospheric ring current and the ionospheric auroral electrojet. Fig. 3 shows the geographical distribution of the correlation coefficient between the observed geomagnetic disturbance and the Dst index, while Fig. 4 shows that in case of northern latitude observatories the auroral electrojet and sometimes the magnetopause currents produced by solar wind pressure impulses are a good candidate.

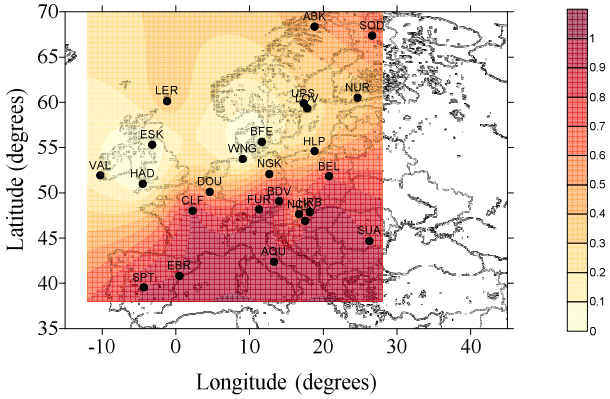

Fig. 3. Correlation coefficient between the Dst index and the horizontal component disturbance at European observatories

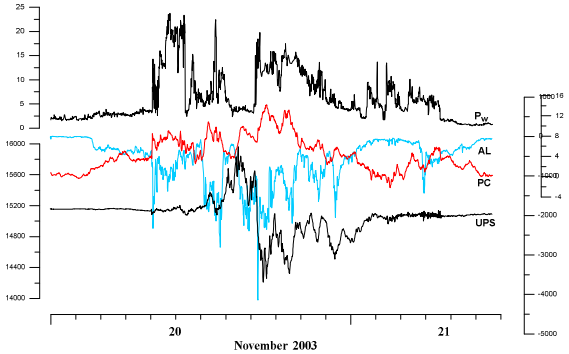

Fig. 4. Evolution of the solar wind dynamic pressure Pw, polar cap currents (PC index), auroral electrojet (AL index), and geomagnetic disturbance at a northern observatory (UPS)

Finally, as a next step in assessing the GIC hazard for the European territory, we calculated the maximum value of the electric field and its orientation at observatories of the network, for each storm considered in this study. Maps are presented in Fig. 5.

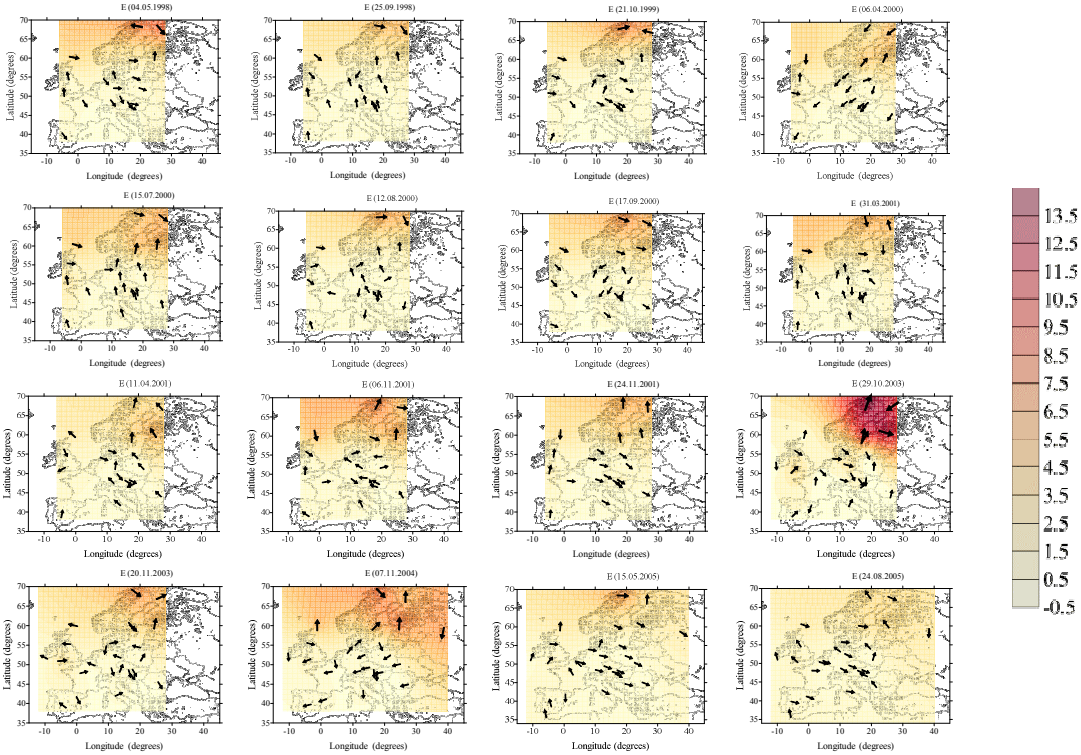

Fig. 5. Maps of the maximum geoelectric field induced at observatories of the European network, for each of the 16 geomagnetic storms of the present study

It is to be noted that the maximum E value is not reached at the same moment at all observatories and its orientation depends on that moment of the storm development. Estimating the actual GICs is an engineering problem and needs knowledge of the power grid.

Instead of conclusion

For future work, we intend to look at local effects and explore the role of magnetopause currents.

Acknowledgements.

The study has been done in the frame of the project CNCSIS – UEFISCDI 93/2011.

References

Matandirotya, E., Cilliers, P. J., Van Zyl, R. R., 2015, Modelling geomagnetically induced currents in the South African power transmission network using the finite element method, Space Weather , doi: 10.1002/2014SW001135.

Viljanen, A. and Pirjola, R., 1989, Statistics on geomagnetically-induced currents in the Finnish 400 kV Power system based on recordings of geomagnetic variations, J. Geomag. Geoelectr., 41, 411-420.

Viljanen, A., Pirjola, R., Pracser, E., Katkalov, J., Wik, M., 2014, Geomagnetically induced currents in Europe, J. Space Weather Space Clim., 4, A09, doi: 10.1051/swsc/2014006.

The Influence of Apr 10, 2001 CME on the Magnetosphere

Diana Beşliu-Ionescu[1], *Marilena Mierla*[2,1], *Georgeta Maris Muntean*[1]

[1] Institute of Geodynamics "Sabba S. Ştefănescu" of the Romanian Academy, Bucharest, Romania
[2] Royal Oservatory of Belgium, Brussels, Belgium
E-mail: diana.ionescu@geodin.ro

Abstract:

Coronal mass ejections (CME) are huge explosions of plasma that could trigger geomagnetic storms. On April 10, 2001 a halo CME was registered by LASCO at 05:30 UT. It was detected into the interplanetary space as an ICME on April 11 at 22:00. The geomagnetic storm associated with this event reached its minimum Dst value one hour later.

We analyse this CME properties and calculate the probability (Srivatsava, 2005) of this (I)CME to have triggered a strong geomagnetic storm. We also investigate the quantity of energy deposited into the magnetosphere during the main phase of this storm using two different formulas by Akasofu (1981) and Wang et al. (2014).

Key words: CME, ICME, geomagnetic storm, energy transfer

1. Introduction

Earth's magnetosphere is the first layer of interaction between solar wind and our technological life. It's form varies with stationary and eruptive phenomena sometimes allowing energetic particles to enter our atmosphere or increase the magnetic field.

Most of the major geomagnetic storms are related to powerful CMEs (e.g. Zhang et al., 2004; Zhao and Webb, 2003), such as the full halo CME from April 10, 2001. The connection between the detection of a CME and the triggering of the geomagnetic storm has been intensively studied (e.g. Gosling, 1993; Gopalswamy et al., 2007). One of the most important property for a CME to be a geo-effective one is its position. This has to be on the Sun's front side and close to the centre.

The prediction of the occurrence of geomagnetic storm is a subject of great interest because of their many side-effects in our lives. There are many methods that scientists use to predict such an event, some pure statistical ones, some of them include modelling and others are pure CME propagation modelling. We chose a semi-empirical model. In order to predict the triggering of intense/super intense geomagnetic storms Srivastava (2005) has implemented a logistic regression model. It combines various CME parameters, to some interplanetary measurements to be correlated with the Dst index.

A very important issue in the occurrence of these storms is the quantity of energy that is transferred from the solar wind to the magnetosphere. We used two different formulas to estimate this energy, that were introduced by Akasofu (1981) and Wang et al. (2014).

We present here the analysis of a CME that was followed by an intense geomagnetic storm, the probability that this CME should have been a geo-effective one and the energy transfer during the following storm.

2. Data Analysis

2.1 CME/ICME

On April 10, 2001 a full halo CME was registered by LASCO at 05:30 UT with a linear speed of 2411 km/s and an acceleration of 211 km/s^2. Its speed at 20 solar radii was 2974 km/s making this CME one of the fastest CMEs of solar cycle 23.

It was triggered by the X2.3 solar flare that started at 05:06 UT, had its maximum at 05:26 and ended at 05:42 UT, in the active region NOAA 9415. This region had an βγδ magnetic classification and it was situated at S22W21. The CME became an interplanetary

coronal mass ejection (ICME) and was registered by ACE on April 11 at 22:00 UT. It was preceded by a sudden concomitant increase in solar wind speed and density. Also the magnitude (B) and the x-component (B_x) of the interplanetary magnetic field had a significant increase.

2.2 Geomagnetic Storm

Figure 1 presents the variation of the Dst index (blue line) along with the magnitude (B) (orange line) and the vertical component of the interplanetary magnetic field (B_z)(green line). The geomagnetic storm associated with the April 10 full halo CME begun with a sudden commencement at 13:43 UT marked by a sudden jump in the Dst time profile of ~20 nT.

This storm's main phase lasted seven hours and, except a small increase around 19:00 UT, it is a smooth decrease to the minimum Dst value of -271 nT at 23:00 UT. The recovery phase lasts a bit more than a day and Dst reaches pre-storm values approximately in the same time as the magnitude of the interplanetary magnetic field (B).

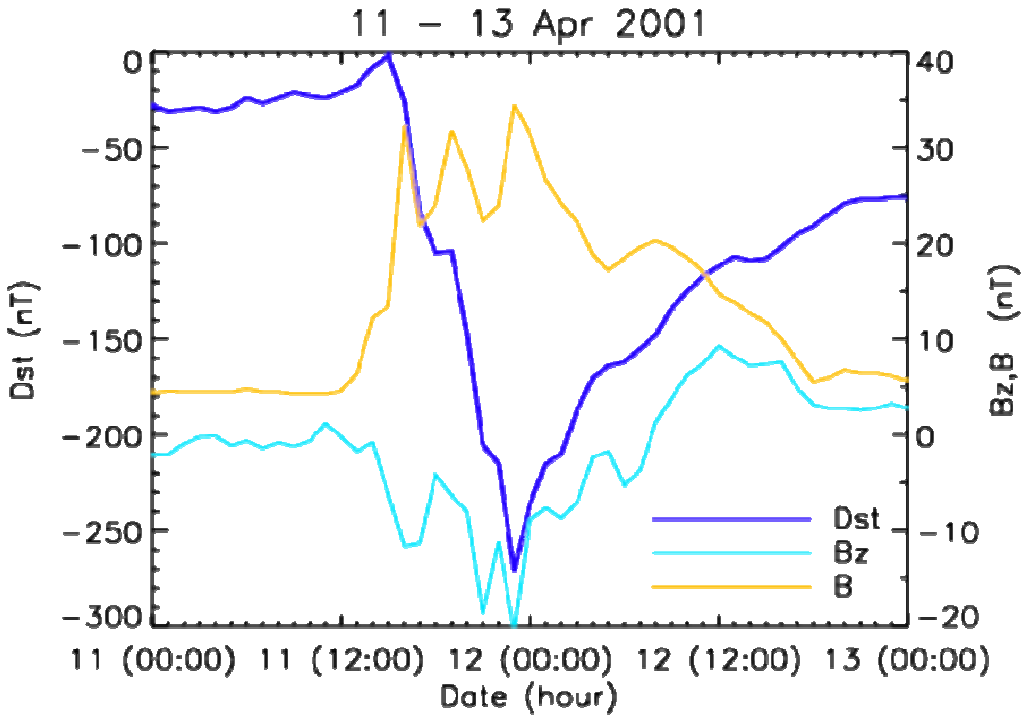

Figure 1: Temporal profiles of Dst, Bz and B during April 11 – 13, 2001

2.3 Probability of the April 10, 2001 CME to have triggered an intense geomagnetic storm

Srivastava (2005) introduced a logistic model to compute the probability of intense and super intense geomagnetic storms to be triggered by CMEs. We modified this model by increasing the number of independent variables from seven to nine, which are now: CME projected speed, acceleration, neutral line orientation, flare importance, position (latitude and longitude), magnetic classification of AR, average magnetic field and the B_z component of the interplanetary magnetic field, and one dependent variable, the Dst index.

The formula introduced by Srivastava (2005) is

$$\Pi = \frac{1}{1 + e^{-Z_i}}, \quad \text{where } Z_i = b_0 + b_1 \times x_{i1} + \ldots + b_j \times x_{ij}$$

where Πi - probability of the occurrence of intense geomagnetic storm given by the i-th observation of the solar variable, b_j (j=0 to J) - model parameters (regression coefficients), x_{ij} (i=0 to I; j=0 to J) - the independent variables. I and J are total number of observations.

In SC23 there were 25 ICMEs to be followed by intense and super-intense geomagnetic storms (-200 nT < Dst < -150 nT, respectively Dst < -200 nT). We have trained the model with 21 events, and used the remaining 4 for validation.

Thus, for April 10, 2001 halo CME we found a 100% probability that this CME should be a geo-effective one.

3. Energy transfer into the magnetosphere

We computed the energy transferred into the magnetosphere during the geomagnetic storm of April 11, 2001 using two different formulas:

the Akasofu empirical parameter (Akasofu, 1981) $\varepsilon = 10^7 V B^2 l_0^2 \sin^4 \frac{\theta}{2}$ [J/s]

and a function obtained by Wang et al. (2013) deducted using a neural network method

$$E_{IN} = 3.78 \times 10^7 n_{SW}^{0.24} V_{SW}^{1.47} B_T^{0.86} (\sin^{2.7} \frac{\theta}{2} + 0.25) \text{ [J/s]}$$

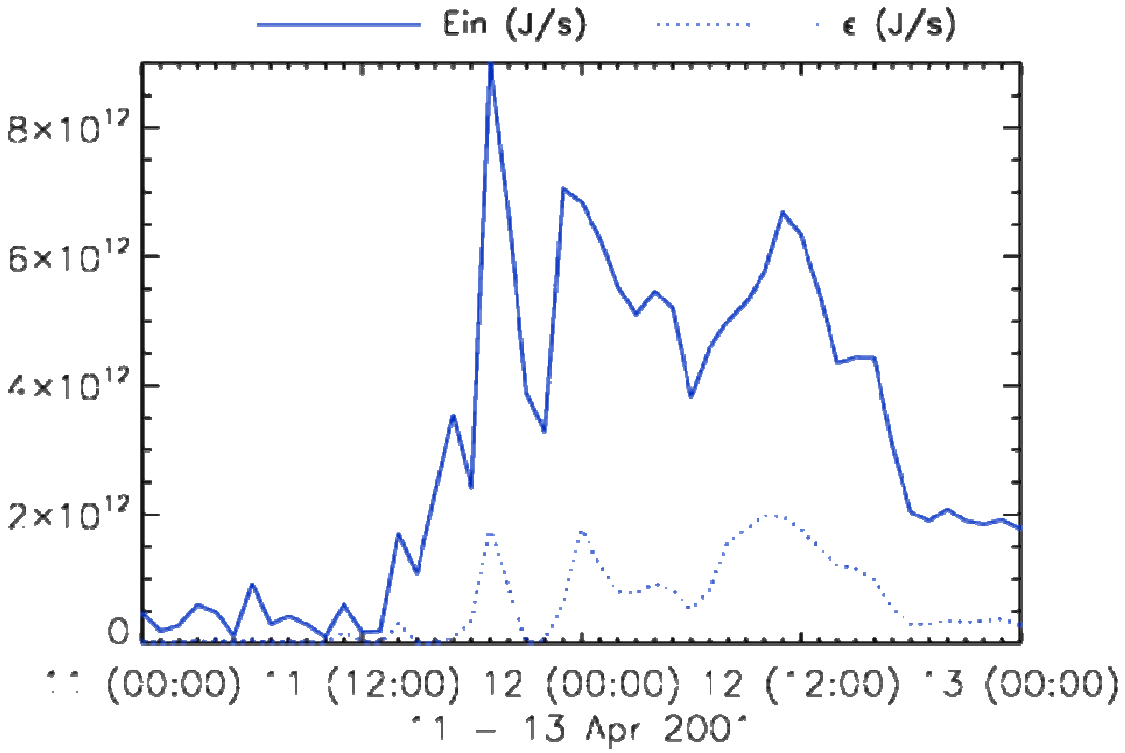

Figure 2: Temporal profiles of ε and EIN during April 11 – 13, 2001

Using the "classical" consideration that the energy is input into the magnetosphere during the main phase of the storm, which in our case is seven hours (Akasofu, 1981), we obtained $W(\varepsilon) = 1.35 \times 10^{17}$ J and $W(E_{IN}) = 1.33 \times 10^{18}$ J. E_{IN} is by one order of magnitude larger than ε, discrepancy that is larger compared to the results obtained by Wang et al. (2014).

Integrating over the entire period that both ε and E_{IN} show a significant increase as compared to a background level – in this case from April 11 at 13:00 UT to April 12 at 18:00 UT – we obtained $W(\varepsilon) = 2.88 \times 10^{18}$ J and $W(E_{IN}) = 1.48 \times 10^{19}$ J.

4. Results and Discussion

We analysed an intense geomagnetic storm that was registered with a minimum Dst on April 11 at 23:00 UT. We presented the characteristics of the triggering coronal mass ejection and its travel towards Earth. We noticed this CME to be situated close to the solar centre. We also analysed the evolution of the geomagnetic storm.

We computed the probability that the April 10, 2001 halo CME should be geo-effective and obtained a 100% certainty.

We noticed that the energy is transferred into the magnetosphere even after the main phase of the geomagnetic storm. We also observed that the two formulas used to calculate this energy transfer have similar temporal profiles, the difference being the magnitude.

Future work should include studying how corrections to the Akasofu parameter change values for the quantity of energy transferred into the magnetosphere.

Acknowledgements:

This research was supported from the CNCSIS project IDEI, No. 93/5.10.2011.

Bibliography

Akasofu, Space Science Reviews, 28, 121-190, 1981
Gopalswamy, N., Yashiro, S., Akiyama, S.: 2007, J. Geophys.Res., 112, A06112
Gosling, J. T., The solar flare myth, J. Geophys. Res., 98, 18937, 1993
Srivatsava, N.: Annales Geophysicae, Volume 23, 2989-2995, 2005
Wang, Y.M., Ye, P.Z., Wang, S., Zhau, G.P., Wang, J., J. Geophys. Res. 107 (A11), 1340, 2002
Wang, G.C., Han, J.P., Li, H., Peng, Z., Richardson, J.D.: J. Geohys. Res., 119, 6199, 2014
Zhang, J., Liemohn, M.W., Kozyra, J.U., Lynch, B.J., Zurbuchen, T.H.: J. Geohys. Res.109, A09101, 2004.
Zhao, X.P., Webb, D.F.: J. Geophys. Res. 108, A6, 2003

Post-Storm High-Latitude Geomagnetic Pc5 Pulsations And Vlf Emissions as A Result of Solar Wind Disturbances

N.G. Kleimenova

Schmidt Institute of the Physics of the Earth RAS, Moscow, Russia
E-mail: kleimen@ifz.ru

Abstract

It is well known that strong solar wind disturbances under southward IMF (Interplanetary Magnetic Field) direction lead to significant space weather violations such as magnetic storms with large geomagnetic activity mainly in the night sector of the auroral latitudes. In the late recovery storm phase, when IMF turns northward and a solar wind energy input stops, the magnetosphere starts to relax, geomagnetic activity drops, but some post-storm effects occur as the different magnetospheric auto-oscillations generation. They get excited mainly in the dayside of the Earth and are observed on the ground. The typical magnetosphere relaxing waves can be the geomagnetic Pc5 pulsations at several minutes period with quasi-monochromatic structure. The main source of these Pc5 pulsations can be the magnetic field line resonance (FLR). Several expressive events of such Pc5 pulsations are shown. The auto-oscillations in the relaxed magnetospheric plasma maser can be observed in the higher frequency band too, namely, as a special regime of the electron-cyclotron instability at several kHz (Very Low Frequency - VLF) emissions, known as quasi-periodic VLF waves. The example of non-typical quasi-periodic picturesque VLF events and their relation with Pc5 pulsations is presented. The trigger of both discussed above processes onset are related with a sudden appearance of some inhomogeneity in the solar wind or IMF.

Introduction

Geomagnetic storms are large disturbances in the Earth's magnetosphere, produced by enhanced solar wind-magnetosphere energy coupling through the magnetic reconnection mechanism. The strong solar wind disturbances under southward Interplanetary Magnetic Field (IMF) direction lead to significant space weather violations with large geomagnetic activity mainly in the night sector of the auroral latitudes. A magnetic storm recovery phase starts with the northward IMF Bz turning and the ring current decay beginning. In this time, solar wind energy input stops, the magnetosphere starts to relax, geomagnetic activity drops, but some post-storm effects occur as the different magnetospheric auto-oscillations generation observed at high latitudes. They get excited mainly in the dayside of the Earth and can be recorded on the ground. Two of them, resonant geomagnetic Pc5 pulsations at frequency range of 1-6 mHz (periods of few minutes) and electromagnetic Very Low Frequency (VLF) emissions at frequency of several kHz, are discussed below.

Geomagnetic pulsations (Pc5 range)

Geomagnetic Pc5 pulsations are typical for storm recovery phase [e.g., Troitskaya et al., 1965; Posch et al., 2003], they exit after ending a last storm main phase substorm (Fig.1). The Pc5 pulsations are attributed to the field line resonances driven by magnetopause shear-flow instability, developing preferentially on the dawn flank. The typical morning Pc5 ground-based pulsations and their spatial geomagnetic latitude (LAT) versus magnetic local time (MLT) distribution are shown in Fig.1. The most likely source for Pc5 pulsations is Kelvin-Helmholtz (KHI) instabilities at the magnetopause generating compressional mode waves that propagate through the magnetosphere and couple to Field Line Resonances (FLR). The cavity mode model [e.g. Samson et al., 1992; Mann et al., 1999] provides a mechanism to convert broadband KHI wave into monochromatic waves corresponded to cavity eigen-frequency. The ability of the cavity to trap waveguide modes as well as KHI exiting is strongly

dependent on the solar wind velocity. Typically, the Pc5 onset generation is caused by an impulse or jump of the solar wind dynamic pressure or an impulsive change in IMF.

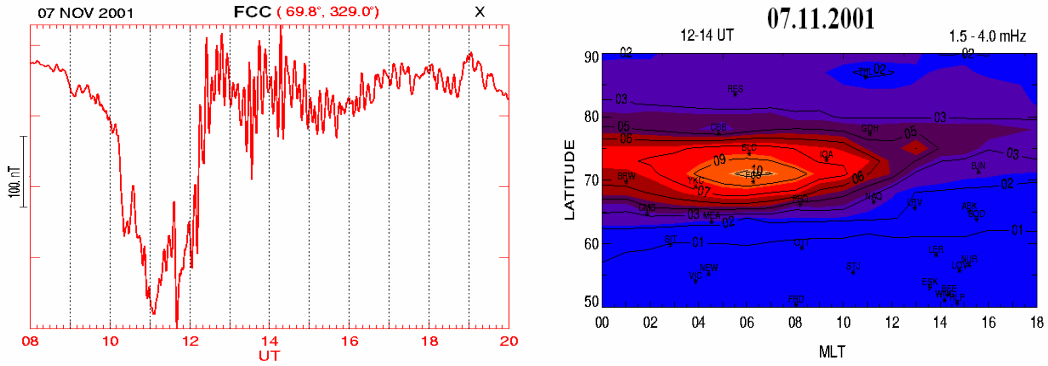

Fig.1. Typical Pc5 geomagnetic pulsations: ground-based magnetogram and LAT-MLT distribution.

The resonant frequency is determined by a field line length, magnetic field strength and the local plasma density. The wave resonant frequency decreases with L-shell increasing. There is an amplitude local peak and phase reversal across the resonant latitude. Such resonant oscillations are usually recorded in high latitudes in the recovery stage of moderate magnetic storms.

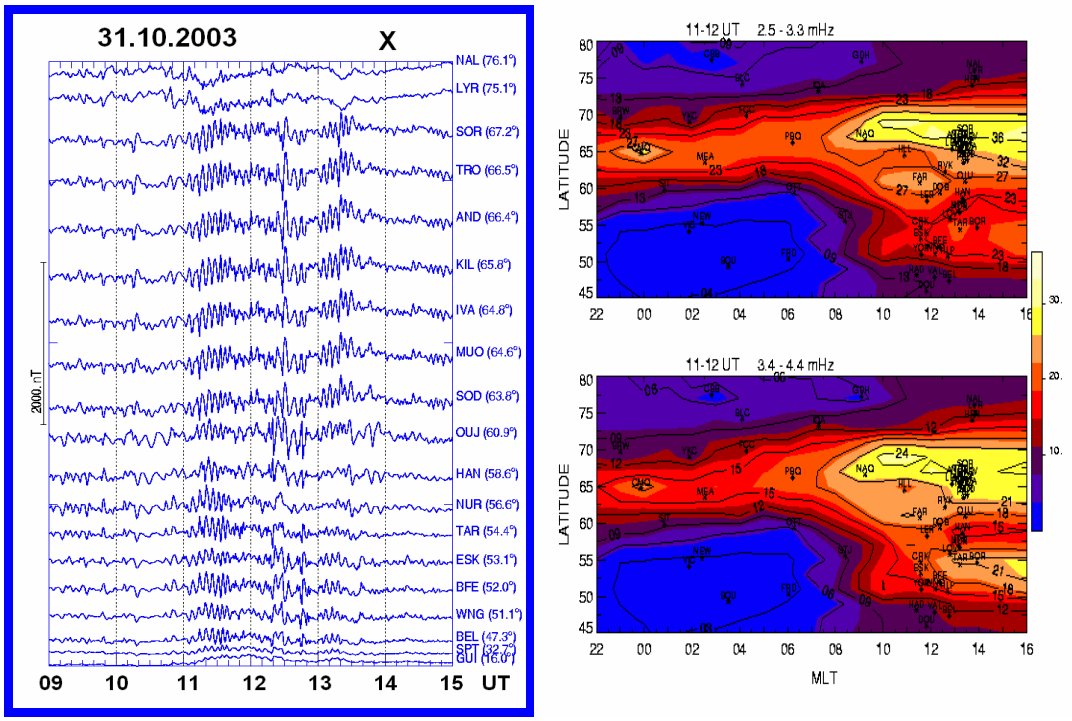

Fig.2. Global Pc5 pulsations in the late recovery phase of the superstorm on 31.10. 2003, magnetograms at different geomagnetic latitudes and LAT-MLT distribution.

After very strong storms and superstorms, caused by huge variations of all solar wind and IMF parameters, the Pc5 pulsations can be observed in global latitude scale (from magnetopause to equator latitudes) [e.g. Kleimenova and Kozyreva, 2007, 2009] sometimes with unusual longitudinal (morning–day) asymmetry. The post-storm intense Pc5 waves can penetrate deep into the inner magnetosphere in the afternoon sector. The nature of these pulsations is still not understand because they do not show a typical local resonance signature. Probably, such post-storm global Pc5 pulsations can be attributed to some eigen-modes of the magneto-hydrodynamic waveguide cavity in the outer magnetosphere due to huge energy stored in the magnetosphere during super storms.

Quasi-periodic VLF-emissions

The auto-oscillations in the relaxed magnetospheric plasma maser can be observed in the higher frequency band too, namely, as a special regime of the whistler mode electron-cyclotron (Very Low Frequency - VLF) emissions at several kHz, known as quasi-periodic (QP) VLF waves (e.g. Manninen et al., 2012, 2013). Note, that typical natural whistler mode electromagnetic emissions (well known as chorus at ~0.5-10 kHz) are generated in the disturbed magnetosphere and do not observed under quiet geomagnetic conditions. The example of typical post-storm QP emissions, observed near high-latitude Scandinavian obs. Sodankyla (SOD), is shown in Fig.3. Such emissions observed more frequently in winter due to better VLF wave reflection from the opposite (summer) hemisphere.

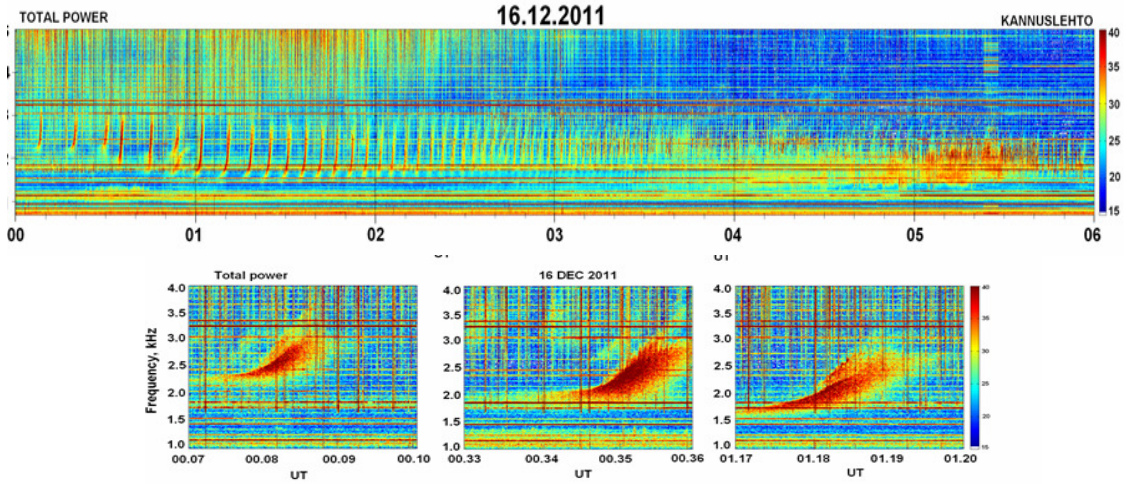

Fig.3. Example of post-storm high-latitude QP emissions: upper panel – 6 hours duration event, bottom one - the 3-min successive intervals of this event.

There is no complete theory, which could adequately explain the observed QP emissions generation. Nevertheless, it is possible to interpret these QP emissions by applying the theory of the auto-oscillation regimes of the cyclotron instability in the magnetospheric plasma maser [Bespalov, 1982; Bespalov and Trakhtengerts, 1986]. According to this theory the primary reason of QP emissions is the auto-oscillations of the radiation belt electrons that correspond to periodic processes of accumulation of energetic particles in the radiation belts and their precipitation into the ionosphere during the electromagnetic emission bursts. The excitation of these oscillations is possible only during low geomagnetic activity. However, one of the necessary conditions for such processes is a transport in the magnetosphere an addition energetic electrons caused by some irregularities in the solar wind and IMF, which usually are observed in that time. The interaction of Pc5 geomagnetic pulsations and hiss VLF emissions is shown in fig.4 and 5. The strange "mushroom" like shape of spectral-temporal VLF hiss variation was observed in the late recovery phase of magnetic storm on 12 December 2013. The cut-off near 2 kHz is a result of the wave propagation in the ionosphere waveguide.

Summary

In the magnetic storm recovery phase, when the solar wind energy input stops, and the magnetosphere starts to relax, the post-storm effects are observed at high latitudes in the dayside as some magnetospheric auto-oscillations such as resonant geomagnetic Pc5 pulsations at frequency range of 1-6 mHz (periods of few minutes) and electromagnetic QP VLF emissions at frequency of several kHz.

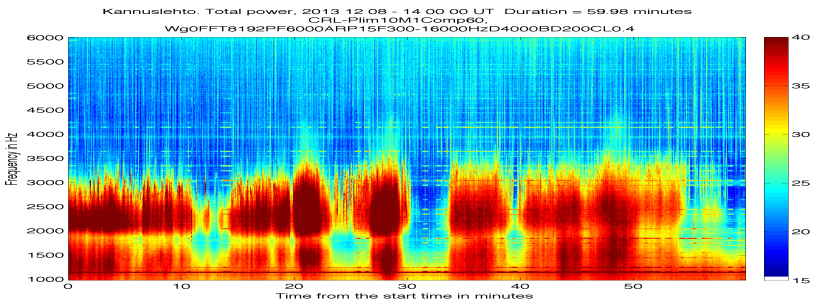

Fig. 4. VLF "mushrooms" at 1-3 kHz at SOD in the storm recovery phase on 08.12.2013.

However, the sequence of individual "mushrooms" could be a result of the modulation of the grow rate of the electron-cyclotron instability by simultaneous resonant Pc5 pulsations (Fig.5). It is seen that each negative Pc5 deviations coincides with a burst of VLF emissions.

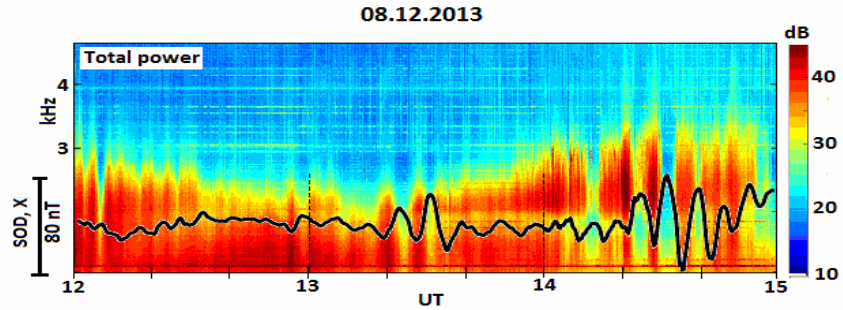

Fig. 5. Modulation of VLFemissions by Pc5 geomagnetic pulsations (black curve).

Acknowledgements. The paper was supported by the RFBR Grants № 13-05-00233 and partly by the Program No 9 of the Presidium of the Russian Academy of Sciences (RAS).

Referances

Bespalov, P.A., Self-excitation of periodic cyclotron instability regimes in a plasma magnetic trap, Physica Scripta, 2/2, 575-579, 1982.

Bespalov, P.A. and Trakhtengerts, V.YuThe cyclotron instability in the Earth radiation belts, Rev. Plasma Physics, 10, 155-292, 1986.

Kleimenova, N.G. and Kozyreva, O.V., Daytime Quasi-periodic geomagnetic pulsations during the recovery phase of the strong magnetic storm of May 15, 2005, Geomagnetism and Aeronomy, 47 (5), 580-587, 2007.

Kleimenova, N.G. and Kozyreva, O.V., Penetration of Pc5 geomagnetic pulsations to unusually low latitudes during the recovery phase of the super-strong magnetic storm of October 31, 2003, Geomagnetism and Aeronomy, 49 (8), 1199–1203, 2009.

Mann, I.R., Wright, A.N., Mills, K.J., and Nakariakov, V.M., Excitation of magnetospheric waveguide modes by magnetosheath flows, J. Geophys. Res., 104, 333-353, 1999.

Manninen, J., Kleimenova, N.G., and Kozyreva, O.V., New type of ensemble of quasi-periodic, long-lasting VLF emissions at the auroral zone, Ann. Geophys., 30, 1655–1660, 2012.

Manninen, J., Kleimenova, N.G., Kozyreva, O.V., Bespalov, P.A., and Kozlovsky, A.E., Non-typical ground-based quasi-periodic VLF emissions observed at L~5.3 under quiet geomagnetic conditions at night, J. Atmos. Solar-Terr. Phys., 99, 123-128, 2013.

Posch, J.L., Engebretson, M.J., Pilipenko, V.A., Hughes, W.J., Russell, C.T., and Lanzerotti, L.J. Characterizing the long-period ULF response to magnetic storms, J. Geophys. Res., 108(A1), 1029, doi:10.1029/2002JA009386, 2003.

Samson, J.C., Harrold, B.G, Ruohoniemi, J.M., Greenwald, R.A., and Walker, A.D.M. Field line resonances associated with MHD waveguides in the magnetosphere, Geophys. Res. Lett. 19, 19441-19444, 1992.

Troitskaya V.A., Melnikova M.V., Bolshakova O.V., Rokityanskaya D.A., Bulatova G.A. Magnetic storms fine structure // Ann. USSR Acad. Sci., Earth physics, 6, 82-86, 1965.

Comparison of substorms during two solar cycles maximum: (1999-2000 and 2012-2013)

I.V. Despirak[1], *A.A. Lubchich*[1], *N.G. Kleimenova*[2]

[1] Polar Geophysical Institute RAS, Apatity, 184209, Russia
[2] Schmidt Institute of the Earth Physics RAS, Moscow, Russia
E-mail: despirak@gmail.com

Abstract:

We presented the comparative analysis of the substorm behavior in the periods of two solar cycles maximum. The substorms, observed during the large solar cycle maximum (1999- 2000, with Wp> 100) and during the last maximum (2012-2013 with Wp~60), were studied. All considered substorms were divided into 3 types according to auroral oval dynamic. First type - substorms which observed only in auroral latitudes ("usual" substorms); second type - substorms which propagate from auroral latitudes (<70º) to polar geomagnetic latitudes (>70º) ("expanded" substorms, according to expanded oval); third type is substorms which observed only at latitudes above ~70º in the absence of simultaneous geomagnetic disturbances below 70° ("polar" substorms, according to contracted oval). Our analysis was based on the 10-s sampled IMAGE magnetometers data, the 1-min sampled OMNI solar wind and interplanetary magnetic field (IMF) data. There were analyzed above 1700 events of "expanded", "polar" and "usual" substorms in 1999- 2000 and in 2012-2013 years. The following substorm characteristics have been studied: (i) the seasonal variations of substorms, (ii) the substorm onset latitude, (iii) the maximal reaching latitude, (iiii) latitudinal range of all three types of substorms. We compare these substorms characteristics and the solar wind conditions observed before substorm onsets.

Introduction

Magnetospheric substorms have long been in the focus of solar□terrestrial physics; however, up to now they still represent an outstanding unresolved problem. In this paper we studied substorms during the large solar cycle maximum (1999- 2000, with Wp> 100) and during the last maximum (2012-2013 with Wp~60). Namely, we present a comparative analysis of some substorms characteristics and the solar wind conditions observed before substorm onsets.

It is noted that although the history of the study substorms is very long, there are only a few large statistical studies of substorms (Borovsky et al., 1993; Tanskanen et al., 2002, 2005; Newell et al., 2001; Frey et al., 2004). Newell et al., 2001 determined 390 substorms events from POLAR UVI, Frey et al., 2004 found more than 2400 substorm events from IMAGE FUV instrument, Tanskanen et al, 2002, 2005 identified more 5000 substorm events from IMAGE magnetometers network. Traditionally, researchers have been considered all substorms. In our work we divided all observed substorms into 3 groups according auroral dynamics. It is known that under normal conditions (moderate disturbance) the auroral oval is located at geomagnetic latitudes about 65-67° ("normal oval"), under quiet conditions (at B_Z>0) the auroral oval shrinks and moves to higher latitudes (>70°GLAT, "contracted oval"), and in disturbed conditions, at increased magnitude of the IMF negative B_Z component, the equatorward boundary of the oval is shifted down to 50° geomagnetic latitude, while its poleward boundary extends to higher latitudes ("expanded oval") (Feldstein and Starkov, 1967). Thus, in our terminology, we call the first type of substorms as "usual" substorms-substorms which observed only in auroral latitudes. Similarly as the auroral oval is called an "expanded" oval, meaning its extension in the disturbed conditions, we will call "expanded" substorms those which start in the auroral zone and then propagate to very high latitudes. We point out that in the maximum phase of "expanded" substorms, the westward electrojet can be

observed at very high geomagnetic latitudes (> 75º) (Despirak et al., 2008). The third type of substorms, we term as "polar" substorms, according to contracted oval. They represent the isolated bay-like magnetic disturbances, observed at geomagnetic latitudes higher than the location of the typical polarward boundary of the auroral oval (> 70° GLAT) and not accompanied or preceded by substorm activity at auroral latitudes.

The aim of this work is the comparison of some substorm characteristics of all three types of substorms and the solar wind conditions observed before substorm onsets during two solar cycles maximum: (1999-2000 and 2012-2013).

Data

We used the magnetic data of the IMAGE meridional chain Nurmijarvi - Ny Alesund, from 57º to 75º of geomagnetic latitudes. The solar wind and Interplanetary Magnetic Field parameters measured by Wind spacecraft were taken from OMNI database. The 1999-2000 and 2012-2013 time intervals, close to two different maximums of the solar activity are used. There were analyzed above 1700 events of "expanded", "polar" and "usual" substorms in 1999- 2000 and in 2012-2013 years.

Results

a) Seasonal variations of substorm number

We calculated the seasonal variations of substorms, observed in two different periods – in 1999-2000 years and in 2012-2013 years. Figure 1 presents the results for 4 different types of substorms: A- all substorms; U- classical (usual) substorms; P- polar substorms; E-expanded substorms.

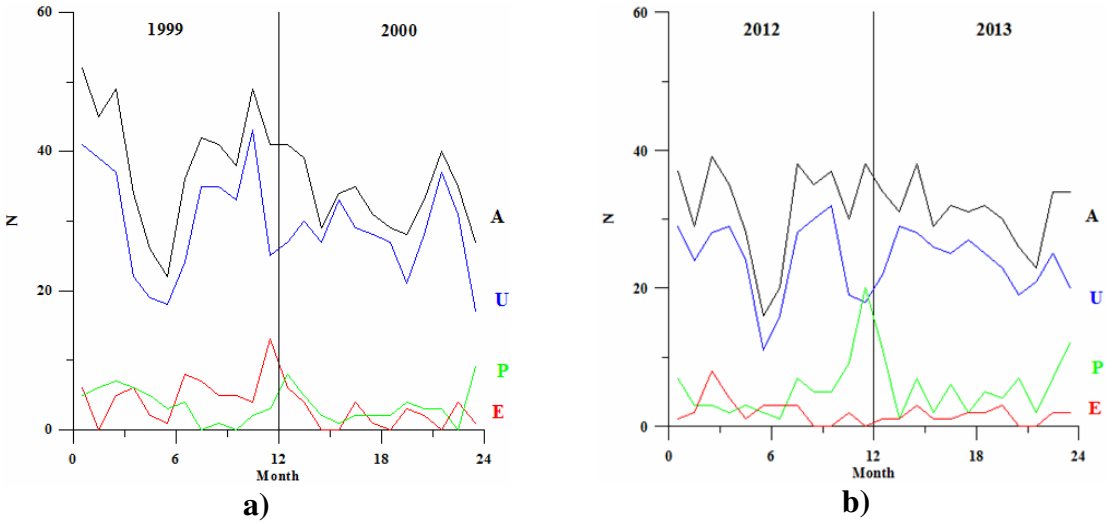

Fig. 1 The results of seasonal variations of substorms during two solar cycle maximums – a)- in 1999-2000 years ; b) – in 2012-2013 years

It is seen that number of substorms is higher during 1999-2000 periods than during 2012-2013 periods; summer minimums of substorms number and spring and autumn maximums are common to both periods; polar substorms behavior was in opposition to other types of substorms. Number of polar substorms have maximum in the winter months; wherein it is noted that expanded substorms maximum was observed in winter 1999-2000, but not observed in winter 2012-2013.

b) the substorm onset latitude and the maximal reaching latitude

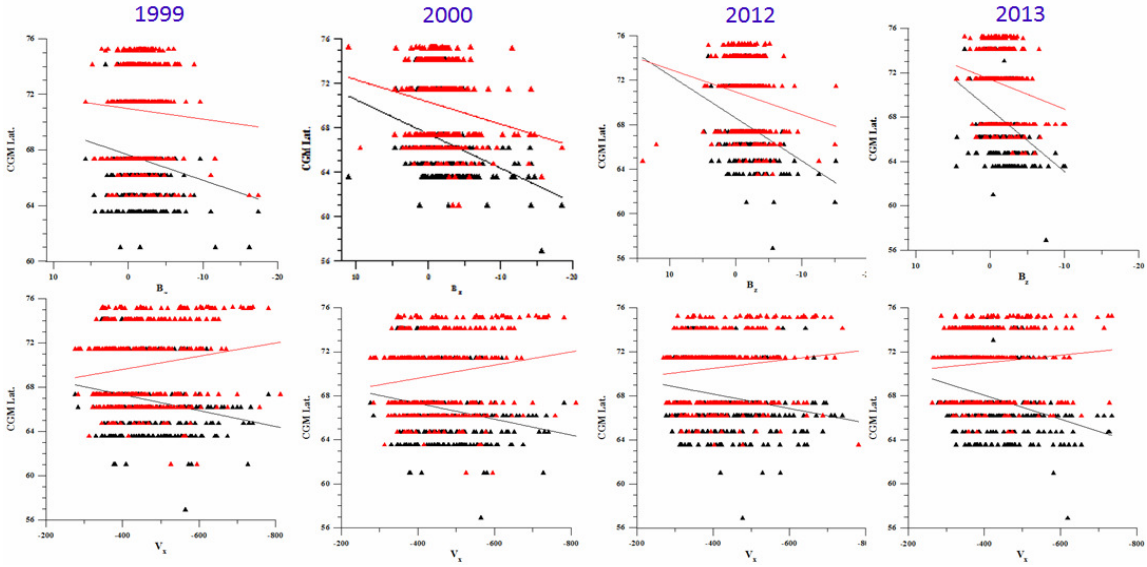

Fig. 2 Substorm onset and maximal reaching latitudes for all substorms during 1999, 2000, 2012 and 2013 periods in dependence on solar wind velosity (V_X) and B_Z component of IMF

c) Solar wind and IMF parameters before substorms onsets

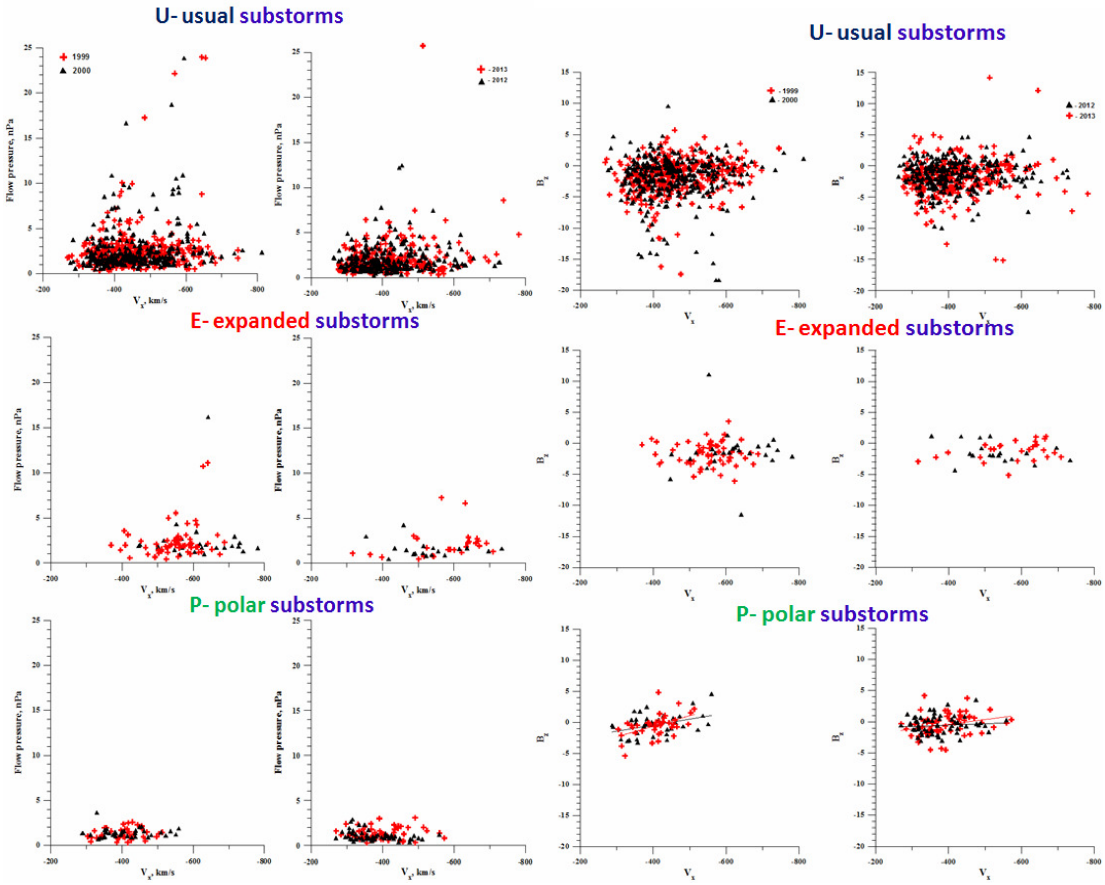

Fig. 3 Parameters of the solar wind and the IMF (B_Z, V_X and P) before substorms onsets for 1999-2000 (left columns) and for 2012-2013 (right columns)

It is shown that significant differences in dependencies on the solar wind parameters (Vx, Bz, P, N, T) between substorms in 1999-2000 and substorms in 2012-2013 not found.

Conclusions

It is shown that:

1. Number of substorms is higher during 1999-2000 periods than during 2012-2013 periods; summer minimums of substorms number and spring and autumn maximums are common to both periods; polar substorms behavior was in opposition to other types of substorms. Number of polar substorms have maximum in the winter months; wherein it is noted that expanded substorms maximum was observed in winter 1999-2000, but not observed in winter 2012-2013.
2. Substorms onset latitudes for 1999-2000 years were a little lower that onset latitudes for 2012-2013 years; the latitudinal sizes of substorms in 1999-2000 years were a little more than the latituinal size of substorms during 2012-2013 years.

Acknowledgment This study was supported by Program No 9 of the Presidium of the RAS. The study is part of a joint Russian - Bulgarian Project 1.2.10 of PGI RAS and IKIT-BAS under the Fundamental Space Research Program between RAS and BAS.

References

Borovsky J.E., R.J. Nemzek, R.D. Belian (1993), The occurrence rate of magnetospheric-substorm onsets: Random and periodic substorms, *J.Geophys.Res*., 105, 3807-3813.

Tanskanen E., T.I. Pulkkinen, H.E.J. Koskinen, J.A. Slavin (2002), Substorm energy budget during low and high solar activity: 1997 and 1999 compared, *J.Geophys.Res*., 107, 1086, doi:10.1029/2001JA900153.

Tanskanen E.I., J.A. Slavin, A.J. Tanskanen, A. Viljanen, T.I. Pulkkinen, , H.E.J. Koskinen, A. Pulkkinen, J. Eastwood (2005), Magnetospheric substorms and strongly modulated by interplanetary high-speed streams, *Geophys. Res. Lett*., 32, L16104, doi:10.1029/2005GL023318.

Newell P.T., K. Liou, T. Sotirelis, C.-I. Meng (2001), Auroral precipitation power during substorms: A Polar UV Imager-based superposed epox analisys, *J.Geophys.Res*., 106, 28885-28896.

Frey H.U, S.B. Mende, V. Angelopoulos, E.F. Donovan (2004), Substorm onset observations by IMAGE-FUV, *J.Geophys.Res*., 109, A10304, doi:10.1029/2004JA010607.

Feldstein, Y.L. and G.V. Starkov (1967), Dynamics of auroral belt and geomagnetic disturbances. *Planet. Space Sci*., 15, 209-229.

Despirak, I.V., A.A. Lyubchich, Kh.K. Birnat, A.G. Yakhnin (2008), Poleward expansion of the westward electrojet depending on the solar wind and IMF parameters. *Geomagn. Aeron.*, 48, no. 3, 284-292.

Substorms observations during two strongly disturbed periods - in March 2012 and March 2015

V. Guineva[1], *I.V. Despirak*[2], *B.V. Kozelov*[2]

[1] Space Research and Technology Institute (SRTI), BAS,
Stara Zagora Department, Stara Zagora, Bulgaria
[2] Polar Geophysical Institute (PGI), Apatity, Russia
E-mail: v_guineva@yahoo.com

Abstract.

In this work two events of strong geomagnetic activity were examined: the period 7-17 March 2012, which is one of the most disturbed periods during the ascending phase of Solar Cycle 24, and the severe geomagnetic storm on 17-20 March 2015. During the first period four consecutive magnetic storms occurred on 7, 9, 12, and 15 March. These storms were caused by Sheath, MC and HSS, and the detailed scenarios for the storms were different. The second event is a storm of fourth level with Kp = 8, the strongest one during the last four years. A geomagnetic storm of such intensity was observed in September 2011. Since then, the level of Kp never exceeded the value 7. Object of our study were the substorms registered during these periods. Observations of the Multiscale Aurora Imaging Network (MAIN) in Apatity have been used. The substorm developments during different storms were compared. Solar wind and interplanetary magnetic field parameters were taken from OMNI data base. Substorm onset time and the subsequent development were verified by data of IMAGE magnetometers network and by data of the all-sky cameras at Apatity. The particularities in the behaviours of substorms connected with different storms during these two interesting strongly disturbed periods are discussed.

Introduction.

It is known that magnetic storms are generated by certain types of solar wind, mainly interplanetary coronal mass ejections (ICME) including Sheath- region ahead and body of ICME (magnetic cloud (MC), and Corotating Ineraction Regions (CIR) between recurrent streams and slower streams (e.g. Gonzales et al., 1990; Tsurutani et al., 2006, Balogh et al., 1999, Burlaga et al., 1982). During solar maxima, most common are the sporadic flows associated with CME (Webb and Howard, 1994), respectively MC (e.g. Burlaga et al., 1982). Recurrent streams and their CIR are more frequent during solar minima. It should be noted that there are differences between storms generated by Sheath, MC and CIR (in intensity, recovery phase duration, etc.) (e.g., Huttunen et al., 2006; Pulkkinen et al., 2007; Yermolaev and Yermolaev, 2006). However there are more complicated storm cases, when the magnetic storms are caused by several sources in the solar wind, coming consecutively one after the other or partly overlapping. Events of strong geomagnetic activity are of special interest because magnetic storms can affect the energetic systems, the space crafts or the ground based systems. That's why coordinated actions of the scientific community are needed to perform and gather observations, to create models of the whole chain of phenomena from the Sun to the Earth in order to make successful predictions of space weather and to prevent failures in the technologic infrastructure by reason of strong geomagnetic storms (Schrijver et al., 2015). Storms are the final effect of the enhanced solar and interplanetary activity. So, it is important to have more observations of substorms during storms, especially under strongly disturbed conditions.

In this paper, two periods of high geomagnetic activity are examined and the observed substorms were studied.

Instrumentation and data used.

Measurements from the Multiscale Aurora Imaging Network (MAIN) in Apatity during two strongly disturbed periods in March 2012 and March 2015 have been used. The all-sky cameras observational system has being built in Apatity since 2008. The cameras characteristics, their mutual situation and the measurement process are described in detail by Kozelov et al. (2012).

Solar wind and interplanetary magnetic field parameters were taken from OMNI data base (http://sdaweb.gsfc.nasa.gov/cdaweb/istp_public/). Kp indices were taken from NOAA database: http://www.ngdc.noaa.gov/stp/GEOMAG/kp_ap.html.

Substorm presence was verified by ground-based data of IMAGE magnetometers network (using meridional chains).

To study the substorm development data from the Apatity all-sky camera (images and keograms) and the Guppy F-044C (GC) camera with field of view ~67° (keograms) were used.

Overview of the interplanetary conditions.

Two time intervals of strong geomagnetic activity were examined: 7-17 March 2012 and 17-20 March 2015.

The time interval 7 – 17 March 2012 (11 days) is one of the first major geomagnetically active periods of the ascending phase of SC24 (Tsurutani et al., 2014). It was examined and the detected features were described (Valchuk, 2013; Tsurutani et al., 2014). Magnetic storms occurred on 7, 9, 12, and 15 March, these are called the S1, S2, S3, and S4 events. These storms were caused by Sheath, MC and HSS, the detailed scenario for all four storms were different.

On 17 March 2015, St Patrick's day, a severe geomagnetic storm (G4) occurred. It was the result of a pair of CME's which left the Sun on 15 March, maybe unexpectedly combined spreading towards Earth and formed a large shock front crossing the Earth orbit. In 4:45 UT the shock wave formed by the CME swept past our planet and a geomagnetic sudden impulse was registered. It coincides with the storm sudden commencement when Dst jumped from 16 to 66 nT. A Magnetic cloud passed the Earth and just after it a HSS superposed and contributed to the storm duration. Dst reached the value -235 nT in 22:47 UT. An overview of the interplanetary conditions during both examined periods is presented in Fig.1.

Results.

The measurements during the periods 7-17 March 2012 and 17-20 March 2015 were examined together with the interplanetary conditions during the measuring periods. 18 substorms were identified over Apatity under clear sky conditions: 10 of them developed during the first period and 8 – during the second one. Three typical cases of substorms were chosen presenting a substorm generated during the main storm phase, a substorm during the recovery phase in the vicinity of the maximal development and a substorm during the late recovery phase.

Case 1. 17 March 2015.

The substorm occurred during the main phase of the severe geomagnetic storm on the same day. Dst was -163 nT. The substorm development is presented in Fig.2 by chosen images of the all-sky camera. The world directions are shown on the first image. UT is written above the images. The substorm was first seen from Apatity in 17:36:40 UT to the South of the station. For some minutes auroras stayed in the South part of the field of view. In 17:42 UT a fast motion towards North was observed and in 17:45:30 UT the auroras occupied the whole field of view.

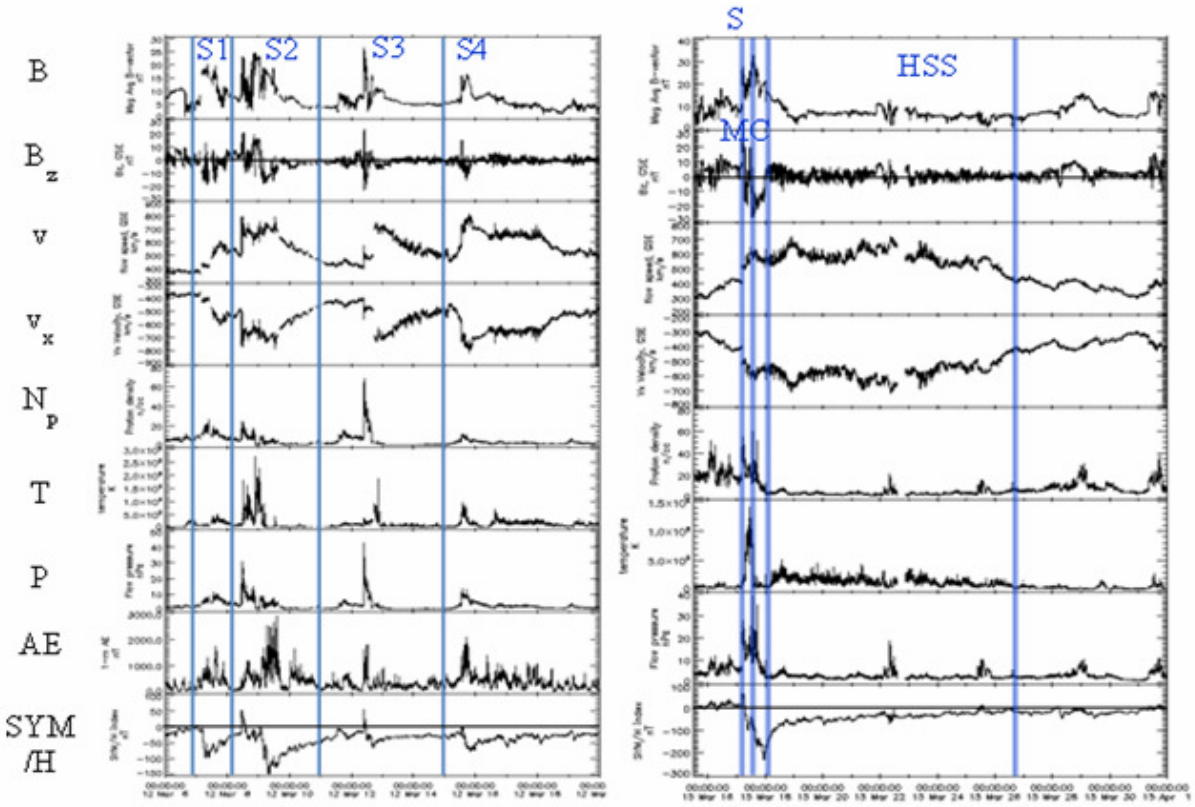

Fig.1. Overview of the interplanetary conditions during the time periods 7-20 March 2012 (to the left) and 16-30 March 2015 (to the right).

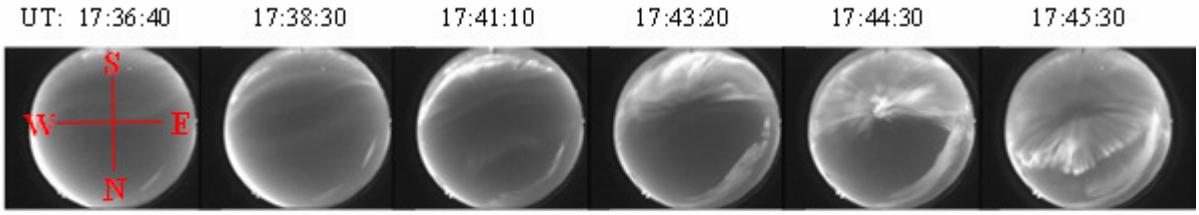

Fig.2. Development of the substorm on 17 March 2015 in 17:36:40 by selected all-sky camera images.

Case 2. 7 March 2012.

The substorm began during the first event of the disturbed interval 7-17 March 2012 during a storm with Dstmin = -98 nT caused by the southward directed sheath fields. In Fig.3. selected images of the all-sky camera are shown. The format is the same as in Fig.2. The substorm developed during the recovery phase of the storm, near the maximal storm development. Dst was -45 nT. Subtsorm auroras appeared in the South part of the field of view in 18:45 UT. The auroras moved towards North, reached zenith in about 18:53 UT and after that auroras surpassed it.

Case 3. 10 March 2012.

The substorm developed during the second event of the disturbed period 7-17 March 2012, when a geomagnetic storm was generated by a MC. Dstmin reached -148 nT. The

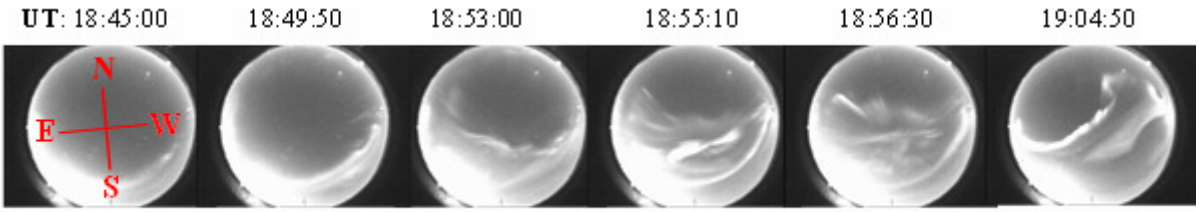

Fig.3. The substorm on 7 March 2012 by all-sky images.

substorm occured in the late recovery phase, Dst was -50 nT. The substorm behavior is presented in Fig.4. The format is the same as in Fig.2. The substorm onset over Apatity was in 18:35:50 UT on 10.03.2012 to the North of the station. The aurora traveled to South, reached zenith in 18:39 UT and moved further to South.

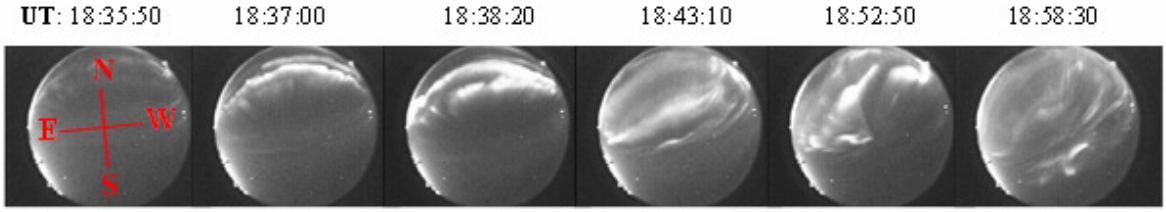

Fig.4. Development of the substorm on 10 March 2012 in 18:35:50 by chosen all-sky images.

Conclusions

It is shown that:

1. Substorms, originated during the main storm phase or near the Dst minimum in the recovery phase, occurred to the South of Apatity, and substorm auroras expanded in North direction;
2. For substorms during the recovery phase or the late recovery phase, auroras were observed near the station zenith or to the North of the Apatity station, and their motion from North to South was registered.

Acknowledgment: This study was supported by Program No 9 of the Presidium of RAS. The study is part of a joint Russian - Bulgarian Project 1.2.10 of PGI RAS and IKIT-BAS under the Fundamental Space Research Program between RAS and BAS.

References:

Balogh A., J.T. Gosling, J.R. Jokipii, R. Kallenbach, H. Kunow (1999), *Space Sci. Rev*., 89, 141-411.

Burlaga L.F., L.F. Klein, L. Sheeley, N.R. Michels, D.J. Howard, R.A. Koomen, M.J. Schwenn, H. Rosenbauer (1982), *Geophys. Res. Lett.* 9, 1317-1320.

Gonzalez W.D., A.L.C. Gonzalez, B.T. Tsurutani (1990), *Planet. Space Sci*. 38, 181-187.

Huttunen K.E.J., H.E.J. Koskinen, A. Karinen, K. Mursula (2006), *Geophys. Res. Lett.* 33, L06107, doi:10.1029/2005GL024894.

Kozelov, B.V., S.V. Pilgaev, L.P. Borovkov, V.E. Yurov (2012), *Geosci. Insrum. Method. Data Syst.*, 1, 1-6,

Pulkkinen T.I., N.Y. Ganushkina, E.I. Tanskanen, M. Kubyshkina, G.D. Reeves, M.F. Thomsen, C.T. Russel, H.J. Singer, J.A. Slavin, J. Gjerloev (2006), *J. Geophys. Res.* 111, A11S17, doi:10.1029/2006JA011627.

Schrijver C.J. et al. (2015), *Adv. Space Res*., 55, 2745-2807

Yermolaev Yu.I., M.Yu. Yermolaev (2006), *Adv. Space Res.* 37, 1175-1181.

Tsurutani B.T., W.D. Gonzalez, A.L.C. Gonzalez, F.L. Guarnieri, N. Gopalswamy, M. Grande, Y. Kamide, Y. Kasahara, G. Lu, I. Mann, R. McPherron, F. Soraas, V. Vasyliunas (2006), *J. Geophys. Res.* 111, A07S01, doi:10.1029/2005JA011273.

Tsurutani B.T., E. Echer, K.Shibata, O.P. Verkhoglyadova, A.J. Mannucci, W.D. Gonzalez, J.U. Kozyra, M. Pätzold (2014), *J. Space Weather Space Clim*., 4, A02, DOI: 10.1051/swsc/2013056

Valchuk T.E., (2013), Astron. Tsirkulyar, N1585, ISSN 0236-2457

Webb D.F., R.A. Howard (1994), *J. Geophys. Res.* 99, 4201-4220.